Cholinergic synaptic plasticity shapes resilience and vulnerability to tau

Kate M. Onuska[1-3], Lauren A. Devito[1], Hayley R.C. Shanks[1], Qi Qi[4], Alycia M. Crooks[1-3], Roy A.M. Haast[2,5,6], Tallulah S. Andrews[7,8], Kayla M. Williams[9,10], Flávio H. Beraldo[2], Ting Qiu[11], Alfonso Fajardo-Valdez[11], Alfie Wearn[9,10], Gary R. Turner[12], Jonathan D. Thiessen[3,13-15], Matthew S. Fox[3,15,16], Justin W. Hicks[3,15], Timothy J. Bussey[2,4], Lisa M. Saksida[2,4], Jennifer Tremblay-Mercier[18], John C.S. Breitner[11,18,19], Jean-Paul Soucy[9], Judes Poirier[11,18,19], Sylvia Villeneuve[9,11,18,19], Vania F. Prado[2,4,17], Marco A.M. Prado[2,4,17], R. Nathan Spreng[9,10,18-20], Taylor W. Schmitz[2-4], for the PREVENT-AD Research Group.

[1]Schulich Medicine and Dentistry, Western University, London, ON, Canada.

[2]Robarts Research Institute, Western University, London, ON, Canada.

[3]Lawson Imaging Research Program, Lawson Health Research Institute, London, ON, Canada.

[4]Department of Physiology and Pharmacology, Western University, London, ON, Canada.

[5]Aix Marseille Univ, CNRS, CRMBM, Marseille, France.

[6]APHM, Hôpital Universitaire Timone, CEMEREM, Marseille, France.

[7]Department of Biochemistry, Western University, London, ON, Canada.

[8]Department of Computer Science, Western University, London, ON, Canada.

[9]McConnell Brain Imaging Centre, Montreal Neurological Institute, McGill University, Montréal, QC, Canada.

[10]Department of Neurology and Neurosurgery, McGill University, Montréal, QC, Canada.

[11]Douglas Mental Health University Institute, Montréal, Canada.

[12]Department of Psychology, York University, ON, Canada.

[13]Division of Medical Physics, CancerCare Manitoba, Winnipeg, MB, Canada.

[14]Department of Radiology, University of Manitoba, Winnipeg, MB, Canada.

[15]Department of Medical Biophysics, Western University, London, ON, Canada.

[16]Department of Physics and Astronomy, Western University, London, Canada.

[17]Department of Anatomy and Cell Biology, Western University, London, ON, Canada.

[18]StoP-Alzheimer Centre, Douglas Mental Health University Institute Research Centre.

[19]Department of Psychiatry, McGill University, Montréal, QC, Canada.

[20]Department of Psychology, McGill University, Montréal, QC, Canada.

Abstract

Synaptic dysfunction is a hallmark of Alzheimer's disease (AD). Yet due to their plasticity, synapses may also adapt to early AD pathology. Using within-participant positron emission tomography scans targeting the vesicular acetylcholine transporter (VAChT) protein, tau, and amyloid in healthy older adults at risk for AD, we show that cholinergic neurons increase presynaptic VAChT levels when colocalized to tau, but not amyloid, with higher responses predicting resilience to cognitive decline over ~10 years. In mice lacking forebrain VAChT, we demonstrate that cholinergic synaptic plasticity plays a causal role in sustaining cognitive flexibility and hippocampal structural integrity. Whole-brain single-nucleus RNA sequencing atlases reveal that cholinergic neurons upregulate a gene-network enriched for synaptic plasticity, with high centrality for the microtubule-associated protein tau (*MAPT*) gene. Our findings identify cholinergic synaptic plasticity as a critical mediator of resilience and vulnerability to tau in presymptomatic AD.

Main

Synaptic dysfunction is among the first detectable features of Alzheimer's disease (AD)[1,2], and the strongest correlate of early cognitive decline[3–7]. However, synapses are also among the brain's most dynamic structures. Synapses can rebalance their strength and connectivity through homeostatic plasticity, a form of cellular adaptation that is thought to underlie the brain's resilience in the face of sustained stress[8–11]. It may even explain how many individuals maintain cognitive function despite years of accumulating AD pathology[12].

Yet whether synapses mount such compensatory responses to specific AD pathologies in the living human brain remains unknown. Prevailing models of AD assume a passive trajectory: β-amyloid (Aβ) and tau pathologies accumulate, circuits fail, and cognition declines. But if synaptic adaptation occurs before neurodegeneration, then it may not only delay decline, but also determine which individuals resist it[13]. The challenge is to capture these early synaptic changes *in vivo*, and disentangle whether they reflect compensation to pathophysiological vulnerabilities.

Here we leverage molecular imaging to quantify cell-type-specific presynaptic function alongside regional tau and Aβ pathology in healthy older adults at elevated risk for AD. We show that basal forebrain (BF) cholinergic synapses mount an adaptive response to early tau pathology, but not Aβ. We demonstrate that this response predicts longitudinal cognitive resilience, modulates tau spreading, and breaks down in individuals who later decline. Supported by transcriptomic and multimodal neuroimaging work across species, our results position cholinergic synaptic plasticity as a homeostatic buffer to tau, and its failure as a tipping point toward neurodegeneration.

Results

Extensive neuropathological staging and neuroimaging work points to the cholinergic BF as one of the first sites of pathology and neurodegeneration in the progression of AD[14–17]. More recent studies have demonstrated that longitudinal BF atrophy in at-risk older adults predicts the progression of cortical neurodegeneration, which reflects the spatial profile of cholinergic presynaptic loss observed in AD patients[18–20]. Parallel lines of evidence suggest that BF cholinergic synapses are essential for promoting Hebbian plasticity[21–26] and stabilizing cellular homeostasis[27–32] in adult neural circuits. Together, these findings suggest that the selective vulnerability of the BF cholinergic projection system may in part be due to early presynaptic adaptations to sustain plasticity and network function under increasing pathological load.

To explore BF cholinergic homeostatic synaptic plasticity in healthy older adults at elevated risk for AD, we collected [^{18}F]-fluoroethoxy-benzovesamicol ([^{18}F]-FEOBV) positron emission tomography (PET) data in individuals enrolled in the PRe-symptomatic EValuation of Experimental or Novel Treatments for Alzheimer's Disease (PREVENT-AD) program (**Table 1**)[33]. [^{18}F]-FEOBV is one of a limited number of PET tracers that permits direct *in vivo* imaging of synapses in humans[34]. It selectively binds to the vesicular acetylcholine transporter (VAChT), a protein exclusively produced by cholinergic neurons and most abundantly expressed within the presynaptic nerve terminals[35]. Because VAChT is responsible for packaging acetylcholine into synaptic vesicles to facilitate cholinergic neurotransmission[36], [^{18}F]-FEOBV uptake provides a cell-type specific measure of cholinergic presynaptic function. To investigate whether adaptations in cholinergic presynaptic function track with early pathological load, we acquired tau ([^{18}F]-AV1451) and β-amyloid (Aβ; [^{18}F]-NAV4694) PET data in each participant (**Extended Data Fig. 1c**).

Table 1 PREVENT-AD Demographic Information

Demographics	**PREVENT-AD**
n	64
Age (at VAChT-PET, Years)	70.53(0.6243)
Females (*n*) %	44(68.75)
APOε4 Carriers (*n*) %	23(35.94)
Education (Years)	15.31(0.3952)
Baseline CDR	0(0)
Baseline MoCA	27.92(0.1867)
Baseline RBANS (Total Score)	101.9(1.154)
Follow-Up RBANS (Total Score)	98.78(1.218)
Baseline to Follow-Up RBANS (Days)	2783(63.22)
RBANS APC (Total Score)	-0.4872(0.1393)
VAChT- to Tau-PET ITI (Days)	517.5(32.18)
VAChT- to Aβ-PET ITI (Days)	508(30.83)

Continuous data are presented as mean(SEM); categorical data are presented as the number of participants(percentage). APC=Annualized Percent Change; APOε4=apolipoprotein-E ε4; CDR=clinical dementia rating; ITI=inter-scan time interval; MoCA=Montreal Cognitive Assessment; PET=positron emission tomography; RBANS=Repeatable Battery for the Assessment of Neuropsychological Status; VAChT=vesicular acetylcholine transporter.

Mapping personalized brain profiles of tau and Aβ

We anticipated that the spatial profiles of tau and Aβ pathology, as well as their potential interdependencies with VAChT, would likely exhibit considerable variation across healthy older adults at risk for AD[37–40]. We therefore adapted a normative deviation mapping approach[41,42] to capture each participant's unique pattern of tau and Aβ pathology in the brain (see *Methods*). Using an iterative, leave-one-out strategy, we generated voxel-wise population median (*M-i*) and scaled median absolute deviation (*MAD-i*) reference images across the cohort, ensuring statistical independence between each participant's PET images and their corresponding reference images. Supporting the robustness of this strategy, we observed consistently high correlations across all pairwise combinations of *M-i* or *MAD-i* reference images (**Extended Data Fig. 2**). For each participant, we identified voxels with tau- or Aβ-PET uptake values falling above or below the 95% confidence interval (CI) of their respective

M-i and *MAD-i* reference voxels. These voxels were classified as regions of high (i.e., >U95) or low (i.e., <L95) pathology, while voxels within the 95% CIs were assigned to intermediate load regions (i.e., L95–M and M–U95) (**Fig. 1a**). Overall, our normative deviation mapping approach identifies individualized profiles of tau and Aβ which are significantly higher or lower than expected in a population of healthy older adults at elevated risk for AD (**Extended Data Fig. 3,4**).

Tau and Aβ may act both independently and synergistically to alter synaptic function[43–46]. We therefore computed the spatial overlap of tau and Aβ pathology within each individual's four pathological load intervals (i.e., <L95, L95–M, M–U95, >U95) to generate three unique profiles of pathology: regions with increasing tau but not Aβ (i.e., Tau~Aβ), regions with increasing Aβ but not tau (i.e., Aβ~Tau), and regions with increasing co-localized pathology (i.e., Tau∩Aβ) (**Fig. 1b**). We then investigated the anatomical distribution and relative concentration of these distinct pathological profiles across individuals, with a focus on regions with high pathology (>U95) that intersect the BF projection zone (BFpz), including the BF, hippocampus, amygdala, and neocortex. Aligning with known early-stage anatomical patterns of pathology[47,48], high Tau~Aβ profiles were found most abundantly in medial and lateral temporal regions (**Fig. 1c**), while high Aβ~Tau profiles were enriched in default mode network hubs (**Fig. 1d**). Profiles of high Tau∩Aβ most frequently appeared in the posterior cingulate and occipitotemporal cortex (**Fig. 1e**). Consistent with prior normative mapping frameworks[41], we also observed that regions of high and low pathology were spatially smaller than intermediate pathology regions (**Fig. 1f–h**). We also verified that tau-PET uptake selectively increased across Tau~Aβ regions, Aβ-PET uptake selectively increased across Aβ~Tau regions, and that both tracers showed progressive increases moving from low to high Tau∩Aβ regions (**Fig. 1f–h**).

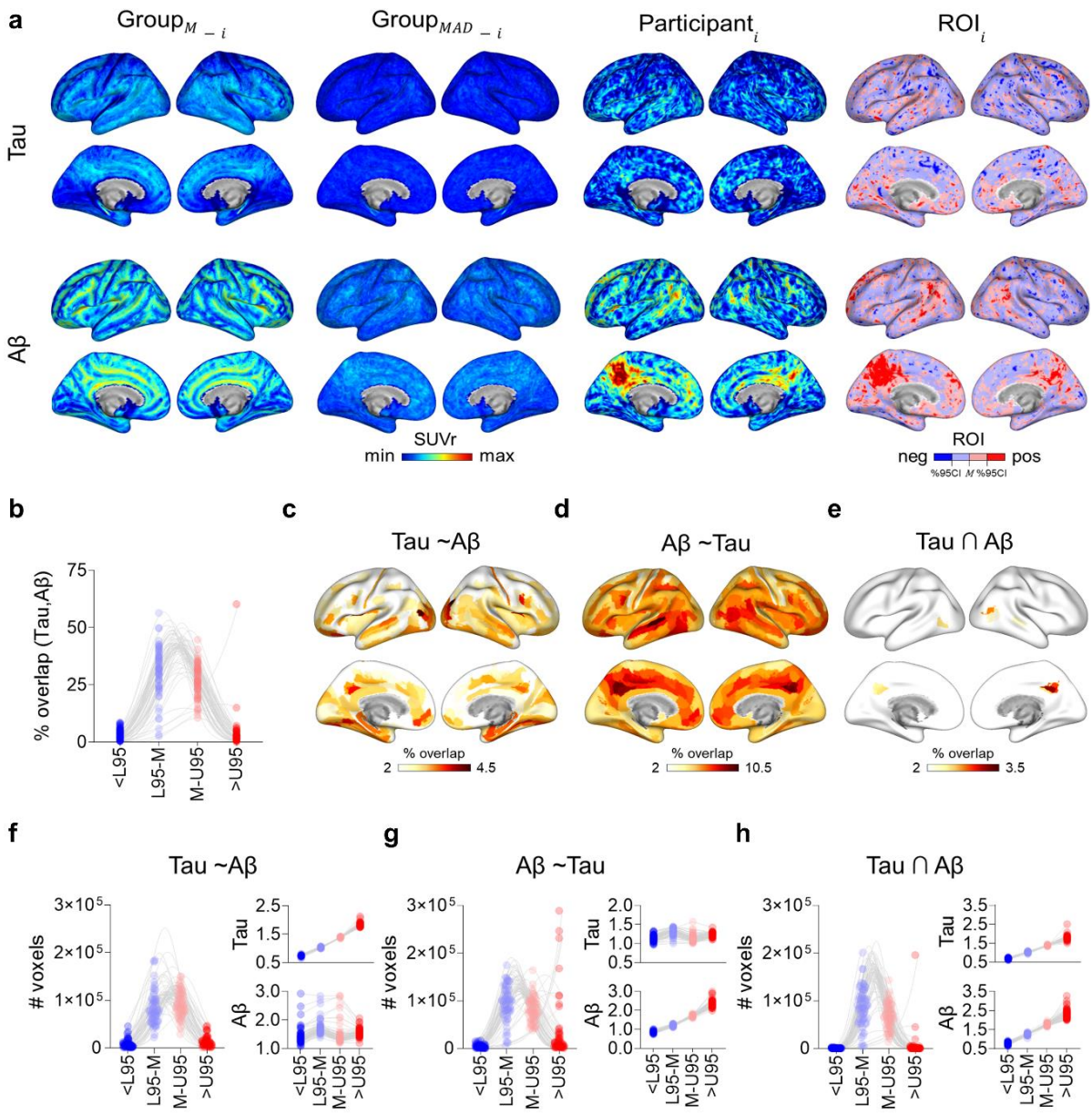

Fig. 1 Individualized mapping of tau and Aβ in healthy older adults at elevated risk for Alzheimer's disease.

a, Representative normative median deviation mapping steps for standardized uptake value ratio (SUVr) Tau-PET (*top*) and Aβ-PET (*bottom*) images. From left to right: (1) population median reference images (Tau$_{M\text{-}i}$: 0.9–2.4; Aβ$_{M\text{-}i}$: 0.9–3), (2) population median absolute deviation images (*MAD-i*: 0–1), (3) corresponding example participant images (Tau: 0.9–2.4; Aβ: 0.9–3), and (4) corresponding example participant segmented CI regions of interest (ROI) (<L95=dark blue; L95–M=light blue; M–U95=light red; >U95=dark red). **b,** Spaghetti plots of

Jaccard index values (percentage) for Tau and Aβ across segmented CI ROIs (One sample Wilcoxon signed-rank test). Colour coding is the same as the ROI_i map in **a**. **c–e,** Mean percentage overlap across participants for Tau~Aβ (**c**), Aβ~Tau (**d**), and Tau∩Aβ (**e**) >U95 ROIs in each parcel of the BFpz, projected on medial and lateral brain surfaces. Parcels are derived from the Human Connectome Project Multi-Modal Parcellation-extended atlas[49]. Darker colours indicate greater overlap of >U95 ROIs with a parcel across participants. **f–h,** Spaghetti plots showing the number of voxels (*left*) and mean SUVrs (*right*) across Tau~Aβ (**f**), Aβ~Tau (**g**), and Tau∩Aβ (**h**) ROIs for each individual (Friedman test followed by Dunn's post-hoc test). Colour coding is the same as the ROI_i map in **a**. Statistical details in **Supplemental Information Table 1**. Source data in **Source Data** file.

Cholinergic synaptic adaptation to tau predicts resilience

In healthy older adults at elevated risk for AD, distinct longitudinal trajectories of cognitive aging may reflect varying degrees of cholinergic homeostatic adaptation to tau and/or Aβ pathology. To interrogate this possibility, we integrated longitudinal neuropsychological data spanning up to 10 years preceding the multi-tracer PET scanning period (**Extended Data Fig. 1a**; Repeatable Battery for the Assessment of Neuropsychological Status (RBANS), see *Methods*) and generated an annualized percent change (APC) score for each participant (stable: APC≥0; decline: APC<0, see *Methods*). We then adjusted the APC values for each participant's age, their baseline cognitive performance, and years of education to produce scores that capture individual deviations from expected cognitive aging (see *Methods*) .

Gaussian mixture modelling revealed two distinct distributions of adjusted APC scores: a vulnerable distribution of individuals exhibiting greater than expected cognitive decline, and a resilient distribution of individuals who maintained their cognitive performance over time (see

Methods) (**Fig. 2a**). No significant differences were detected between vulnerable and resilient subgroups in terms of age, biological sex, or apolipoprotein-ε4 (*APOε4*) carriership (**Table 2**). We also did not observe significant between-group differences in baseline cognition (**Fig. 2a**) or years of education (**Table 2**).

Table 2 Resilient and Vulnerable Subgroup Comparisons

Demographics	**Resilient**	**Vulnerable**	**Statistic**	***P*-value**
n	52	12		
Age (VAChT-PET, Years)	70.60(68.40-72.61)	69.04(67.82-71.05)	*U*=268	0.4576
Females (*n*) %	35(67.3)	9(75.0)		0.7385
Apoε4 Carriers (*n*) %	16(30.7)	7(58.3)		0.0985
Education (Years)	15(14-17)	15(13-17)	*U*=284.5	0.6409
Baseline RBANS (Total Score)	101.2(1.295)	104.6(2.485)	*t*=1.136	0.2602

Age and education are shown as median(95CI). RBANS total score is presented as mean(SEM). Categorical data are given as the number of participants(percentage). Age and education were assessed with a two-sided Mann-Whitney U test. Two-sided independent samples t-test was used to evaluate RBANS total score. Fisher's exact test was used to assess differences in categorical variables. APOε4=apolipoprotein-E ε4; PET=positron emission tomography; RBANS=Repeatable Battery for the Assessment of Neuropsychological Status; VAChT=vesicular acetylcholine transporter.

We next asked whether the resilient and vulnerable subgroups differed according to their individual profiles of tau and/or Aβ. To do this, we compared the size of the high (>U95) Tau~Aβ, Aβ~Tau, and Tau∩Aβ regions between groups[50,51]. Consistent with an increased spatial extent of pathology, the vulnerable subgroup exhibited significantly larger Tau~Aβ (**Fig. 2b**), Aβ~Tau (**Fig. 2c**), and Tau∩Aβ (**Fig. 2d**) regions than the resilient group. We then compared VAChT levels between resilient and vulnerable groups in each of these regions. Here, we observed that the resilient subgroup exhibited significantly higher VAChT levels in Tau~Aβ (**Fig. 2e**) and Tau∩Aβ (**Fig. 2g**) regions relative to vulnerable individuals. However, VAChT levels did not significantly differ between subgroups in areas defined only by high Aβ pathology (**Fig. 2f**). These findings suggest that tau may more directly affect presynaptic cholinergic function than Aβ.

Do the observed group differences in VAChT reflect tau-associated cholinergic synaptic loss in vulnerability, tau-mediated VAChT upregulation in resilience, or both? To investigate these possibilities, we performed voxel-wise regressions between each individual's profile of tau and VAChT in the BFpz, while covarying for Aβ (**Fig. 2h**). This approach allowed us to isolate fine-grained co-fluctuations in the spatial relationship between tau and VAChT. We found that tau-mediated changes in VAChT varied in both direction and magnitude across the cohort (**Fig. 2i**), with a significant skew toward positive associations, consistent with an upregulation of VAChT to tau.

To verify that [^{18}F]-FEOBV is capable of detecting endogenously driven increases in VAChT, we performed [^{18}F]-FEOBV microPET imaging in a *BAC*-transgenic mouse line with global overexpression of synaptic VAChT (HYP[52]) and wild-type (WT) controls (**Extended Data Fig. 5a**). We found that HYP mice exhibited on average ~20% higher [^{18}F]-FEOBV uptake throughout the BFpz relative to WT mice (**Extended Data Fig. 5b**). In a subset of these mice, we further demonstrated that [^{18}F]-FEOBV uptake values closely tracked with VAChT protein levels in the cortex and hippocampus (**Extended Data Fig. 5c**). In humans, [^{18}F]-FEOBV uptake increased by ~4.7% per standard deviation increase in tau (**Fig. 2i**), a response magnitude well within the dynamic range observed in VAChT overexpressing mice.

If tau-colocalized upregulation of presynaptic VAChT reflects a functionally adaptive response, it should be associated with smaller spatial extents of tau pathology in the BFpz and less cognitive decline over time. Consistent with this hypothesis, stronger tau-VAChT coupling was linked to reduced high (>U95) Tau~Aβ coverage (**Fig. 2j**) and more stable longitudinal cognition scores (**Fig. 2k**).

We then evaluated the predictive utility of tau-VAChT coupling for classifying resilient and vulnerable subgroups. Here, we found that individual tau-VAChT coupling coefficients effectively distinguished the groups with an area under the curve (AUC) of 0.80. At this threshold, tau-VAChT coupling corresponds to a ~1.1% increase in VAChT per standard deviation increase in tau (**Fig. 2l**). As a comparison, we tested whether direct coupling between tau and Aβ while adjusting for VAChT could also determine subgroup membership. However, this model produced a substantially lower, nonsignificant AUC (0.64) (**Fig. 21**). These results suggest that the relationship between tau and VAChT, rather than tau and Aβ, is a robust predictor of individual cognitive aging trajectories in healthy older adults at risk for AD.

Although the linear relationship between VAChT and tau in the BFpz distinguishes resilient from vulnerable individuals (**Fig. 2i–l**), these trends do not capture regions where VAChT is disproportionately higher or lower relative to levels of colocalized tau. To quantify these divergences, we applied our normative deviation mapping approach to the VAChT-PET dataset (see *Methods*, **Extended Data Fig. 2** and **Extended Data Fig. 6**). We then examined the spatial overlap between VAChT and tau under two distinct models of potential alignment: an adaptive model (VAChT > tau), and a lag-loss model (tau > VAChT) (**Fig. 2m**). Resilient individuals exhibited significantly greater overlap under the adaptive model, whereas vulnerable individuals showed significantly greater overlap under the lag-loss model (**Fig. 2m**). We then examined where in the brain these distinct patterns are most strongly expressed. At the group level, both models exhibited highest overlap in temporal and precuneus regions, indicating a common core brain network expressing strong tau-VAChT colocalization (**Extended Data Fig. 7a,b**). However, resilient and vulnerable individuals showed opposite load level-dependent profiles of tau and VAChT within these areas (**Fig 2n,o**). Together, our findings

indicate that where presynaptic VAChT and tau colocalize, VAChT levels tend to overshoot tau in the resilient brain, and undershoot tau in the vulnerable brain.

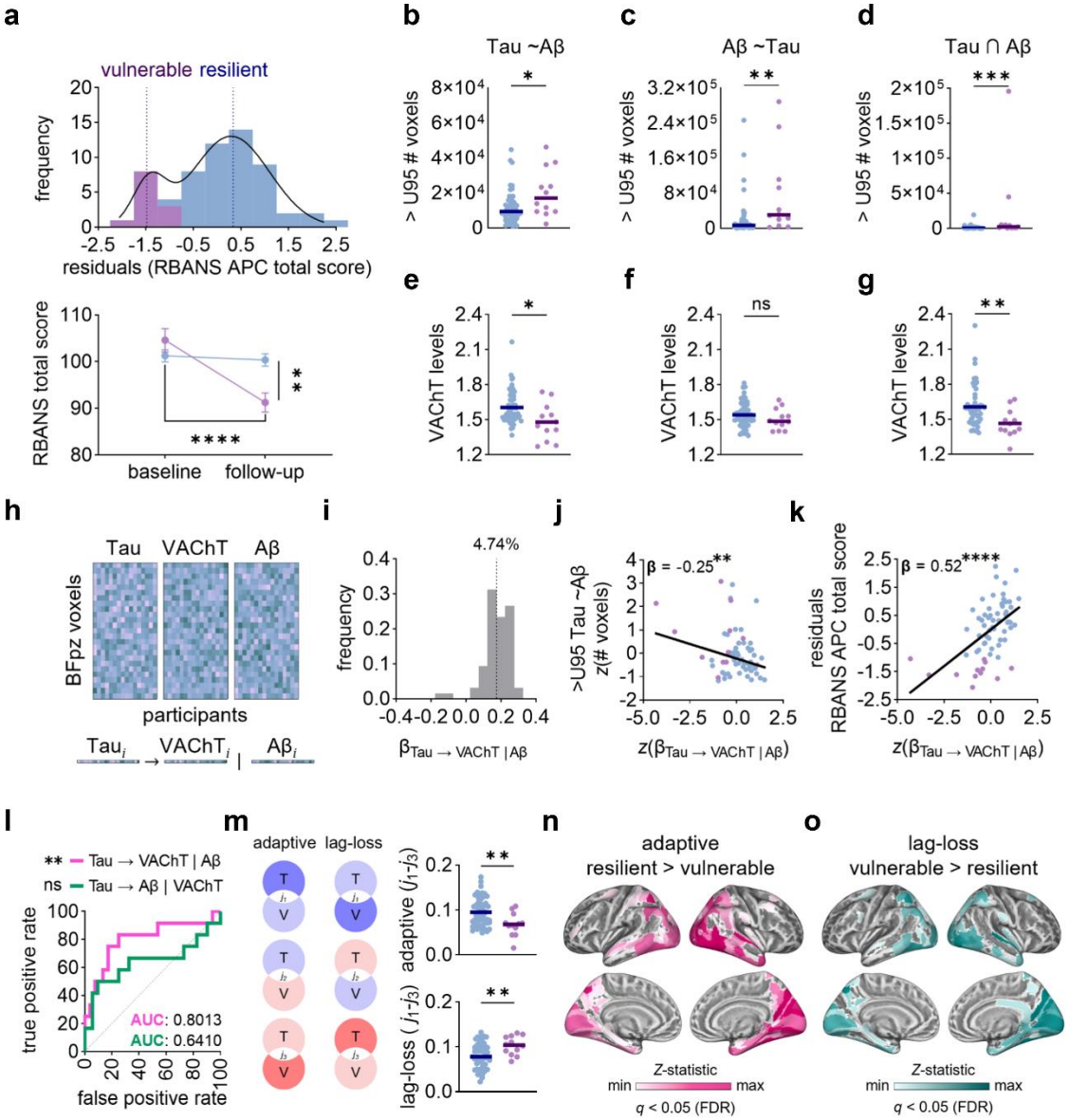

Fig. 2 Cholinergic synaptic adaptation to tau confers cognitive resilience.

a, (*top*) Resilient (*n*=52, blue) and vulnerable (*n*=12, purple) subgroups identified from Gaussian Mixture Modelling (GMM) of adjusted RBANS APC total scores. The dotted lines indicate subgroup means. (*bottom*) RBANS total scores at baseline and follow-up visits, split by subgroup (Mixed-effects model followed by Fisher's LSD). **b–d,** Plots showing the number of voxels in high (>U95) Tau~Aβ (**b**), Aβ~Tau (**c**), and Tau∩Aβ (**d**) regions for resilient (blue)

and vulnerable (purple) subgroups (median; two-sided Mann-Whitney U tests). **e–g,** Plots showing VAChT standardized uptake value ratio (SUVr) levels in the above regions. Subgroup colour coding is the same as **b–d** (median; two-sided Mann-Whitney U tests). **h,** Schematic of within-participant regression analyses. For each participant, individual (*i*) voxel-wise profiles of Tau-PET, VAChT-PET, and Aβ-PET within the BFpz were used to compute the linear relationship between tau and VAChT, while covarying for Aβ ($\text{Tau}_i \rightarrow \text{VAChT}_i \mid \text{A}\beta_i$). **i,** Histogram of individual tau-VAChT regression coefficients (β). Line indicates the mean. **j,** Scatter plot showing the linear association between tau-VAChT coupling estimates from **i** and the number of voxels in high (>U95) Tau~Aβ regions (linear model with robust regression). **k,** Scatter plot showing the linear association between tau-VAChT coupling estimates from **i** and adjusted RBANS APC total scores (linear model with robust regression). **l,** Receiver-operating curves (ROCs) generated using regression coefficients to classify resilient and vulnerable subgroups (pink: Tau → VAChT | Aβ; green: Tau → Aβ | VAChT). **m,** Schematic of adaptive (*left*) and lag-loss (*right*) models of spatial overlap between tau and VAChT. Plots show mean Jaccard similarity coefficients from each model for resilient (blue) and vulnerable (purple) subgroups (median; two-sided Mann-Whitney U tests). **n,o,** *Z*-statistics from subgroup comparisons of adaptive (**n**, min-max: 2.39–4.55) and lag-loss (**o**, min-max: 2.52–3.84) model expression in BFpz parcels, displayed on medial and lateral brain surfaces. Parcels are derived from the Human Connectome Project Multi-Modal Parcellation-extended atlas[49] (two-sided Wilcoxon rank-sum test; adjusted for the false-discovery rate (FDR) at 5%). Statistical details in **Supplemental Information Table 1**. **P*≦0.05, ***P*≦0.01, ****P*≦0.001, *****P*≦0.0001, ns,not significant. Source data in **Source Data** file.

Cholinergic synapses support cortical integrity and cognition

Our findings thus far indicate that cholinergic synapses selectively adapt to increasing tau

pathology, and that a lack of cholinergic synaptic responsivity is associated with a profile of longitudinal cognitive decline and increased vulnerability to tau spreading. To more directly investigate whether a constraint on cholinergic presynaptic function causally affects brain structure and function, we performed *in vivo* multimodal imaging and cognitive profiling in adult (6–7-month-old) WT mice and mice with a conditional knock-out (KO) of forebrain VAChT[27,53].

In KO mice, VAChT protein expression is selectively eliminated from forebrain cholinergic neurons through *Cre*-dependent recombination. Biochemical analyses confirmed that VAChT protein levels were severely reduced in KO mice in cortical and hippocampal targets of the cholinergic BF, as well as striatal cholinergic interneurons, whereas regions innervated by brainstem cholinergic neurons remained intact (**Fig. 3a**). To extend these findings *in vivo*, we performed [^{18}F]-FEOBV microPET imaging in both KO and WT mice. Consistent with the selective elimination of VAChT in forebrain cholinergic neurons, KO mice exhibited reduced forebrain [^{18}F]-FEOBV uptake relative to WT mice, with no corresponding differences observed in the brainstem (**Fig. 3b**).

To assess cognitive function under normal or reduced forebrain VAChT conditions, WT and KO mice performed a pairwise visual discrimination and reversal (PVD-PVR) touchscreen task of cognitive-flexibility (**Fig. 3c**, see *Methods*). During PVD testing, both WT and KO mice performed significantly above chance (>50% correct) at target detection. However, consistent with a causal role for cholinergic synaptic plasticity in updating learned associations[54–56], forebrain VAChT KO mice exhibited a sustained impairment during reversal testing (PVR), whereas WT mice successfully achieved reversal learning (**Fig. 3d**). We further demonstrated that partial restoration of acetylcholine bioavailability in KO mice via continuous

administration of an acetylcholinesterase inhibitor (donepezil; 1.5 mg kg^{-1}) significantly improved PVR task performance to above chance levels (**Fig. 3d**).

Does a targeted disruption of forebrain cholinergic presynaptic function impact neuronal integrity in downstream targets? To address this question, we performed whole-brain *in vivo* 9.4T structural magnetic resonance imaging (MRI) in KO and WT mice. We then applied voxel-based morphometry to quantify grey matter volume differences between the groups. Compared to WT mice, we observed significantly lower grey matter volume across multiple BFpz regions in KO mice, with the most pronounced reductions observed in the hippocampus (**Fig. 3e**). We additionally confirmed in age-matched *Cre*-only expressing mice that the observed changes in hippocampal structural integrity were not due to off-target recombination events (**Supplemental Information Table 2**). These findings further reinforce the critical contributions of BF cholinergic presynaptic function to the mechanisms supporting both cognition and neuronal health.

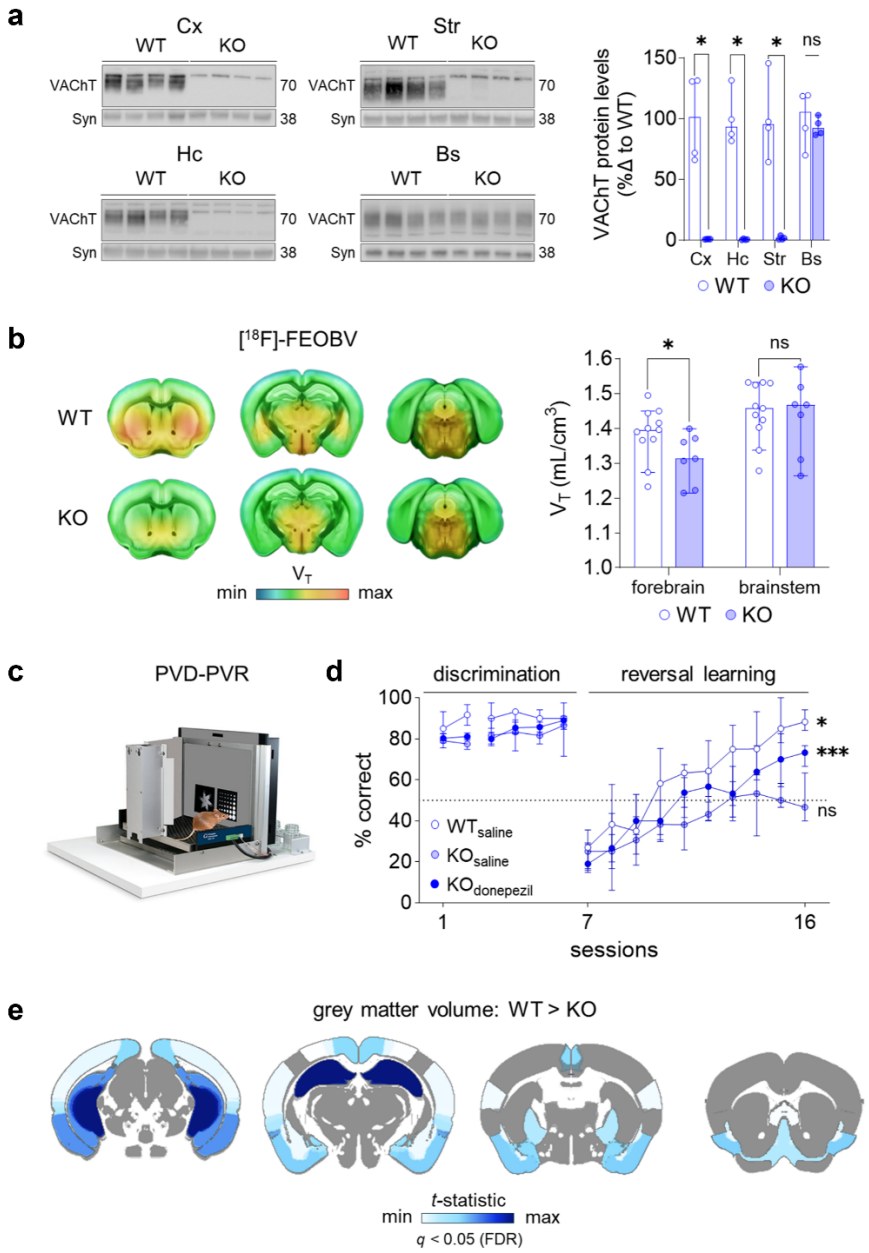

Fig. 3 Loss of forebrain VAChT impairs cognitive flexibility and induces hippocampal neurodegeneration in mice.

a, VAChT and synaptophysin (Syn) protein levels in WT (n=4) and KO (n=4) mice from cortical (Cx), hippocampal (Hc), striatal (Str), and brainstem (Bs) tissue samples (median±95%CI; two-sided Mann-Whitney U test). **b,** Average [^{18}F]-FEOBV total volume of distribution (V_T) brain profiles in WT (n=11) and KO (n=7) mice, overlaid on coronal sections of the mouse brain (min-max: 0.3–2.1). Forebrain and brainstem [^{18}F]-FEOBV V_T values in

WT and KO mice (median±95%CI; two-sided Mann-Whitney U test). **c,** Schematic of mouse pairwise-visual discrimination/reversal (PVD-PVR) touchscreen task. **d,** PVD-PVR task performance (% correct trials) in saline-treated WT (n=6) and KO (n=8) mice, and donepezil-treated KO mice (n=11). PVD (Sessions 1–6) and PVR (Sessions 7–16) testing sessions shown, and the dotted line indicates chance (50%) performance (median±IQR; two-sided one sample Wilcoxon signed-rank test). **e,** Between-group comparisons of regional grey matter volume in the BFpz (WT: n=14, KO: n=10). Regions from the Allen Mouse Brain Atlas common coordinate framework version 3[57] overlaid on coronal sections of the mouse brain, thresholded and colour-coded by t-statistic (two-sided independent samples t-tests; adjusted for the false-discovery rate (FDR) at 5%). Statistical details in **Supplemental Information Table 1**. Example mouse data displayed using MRIcroGL: https://www.nitrc.org/projects/mricrogl. *P≦0.05, ***P≦0.001, ns,not significant. Source data in **Source Data** file.

Cholinergic synaptic plasticity is *MAPT*-centric

The selective pattern of grey matter volume loss observed in forebrain VAChT KO mice led us to hypothesize that regional vulnerability may reflect underlying differences in the expression of gene networks prone to dysregulation in AD. To test this hypothesis, we examined the spatial correspondence between regional grey matter volume differences in WT and KO mice and regional gene expression profiles in the healthy adult mouse brain (**Fig. 4a**)[58]. We focused on an *a priori* defined gene network enriched for presynaptic functions, including neurotransmitter secretion and synaptic plasticity, that is known to be differentially expressed in cortical neurons vulnerable to AD pathology and neurodegeneration[59]. We found that regions exhibiting greater grey matter loss in KO mice also showed higher intrinsic expression of this plasticity-related gene network (**Fig. 4b**), and that this association exceeded chance levels under spatially constrained null models (**Fig. 4c**)[60].

To better understand the cellular basis of this relationship, we cross-referenced the expression of the plasticity gene-network in whole brain single-nucleus RNA sequencing (snRNAseq) atlases derived from the healthy adult mouse[61] and healthy adult human brain[62]. This strategy enabled us to systematically survey the network's expression in virtually every class of neurons in the telencephalon. Spatial clustering by plasticity gene-network expression in all neuronal groups in the telencephalon are shown for mice (**Fig. 4d**) and humans (**Fig. 4e**), colour coded according to their dominant neurochemical profile (i.e., glutamatergic, GABAergic, cholinergic, other). For each neuronal cluster, we then computed a network expression score using the differentially expressed genes that overlapped with the network. Consistent with a convergence between synaptic plasticity and vulnerability, we found that cholinergic neurons in both the adult mouse (**Fig. 4f**) and human (**Fig. 4g**) brain ranked in the top 25% of neuronal clusters exhibiting significant network upregulation. We further confirmed that these cholinergic neurons most likely originated from the BF based on their unique transcriptional profiles. Other neurons which highly upregulated this gene-network included BF GABAergic neurons and glutamatergic neurons from cortical, hippocampal and amygdalar areas (**Fig. 4f,g**).

We next explored which genes are most central to this network. To do so, we re-weighted the significant edges from the original functional network[59] by the expression values of overlapping genes in BF cholinergic neurons (see *Methods*). In both mice and humans, we found that the microtubule-associated protein tau (*MAPT*) gene exhibited a high degree of network centrality (**Extended Data Fig. 8**). To illustrate the gradient of *MAPT* expression across all telencephalic neuronal clusters, we mapped the raw *MAPT* expression values to the same low dimensional spaces as in (**Fig. 4d,e**). We identified that BF cholinergic neurons are

among the neuronal groups with the highest *MAPT* expression in both the adult mouse (**Fig. 4h**) and human (**Fig. 4i**) telencephalon.

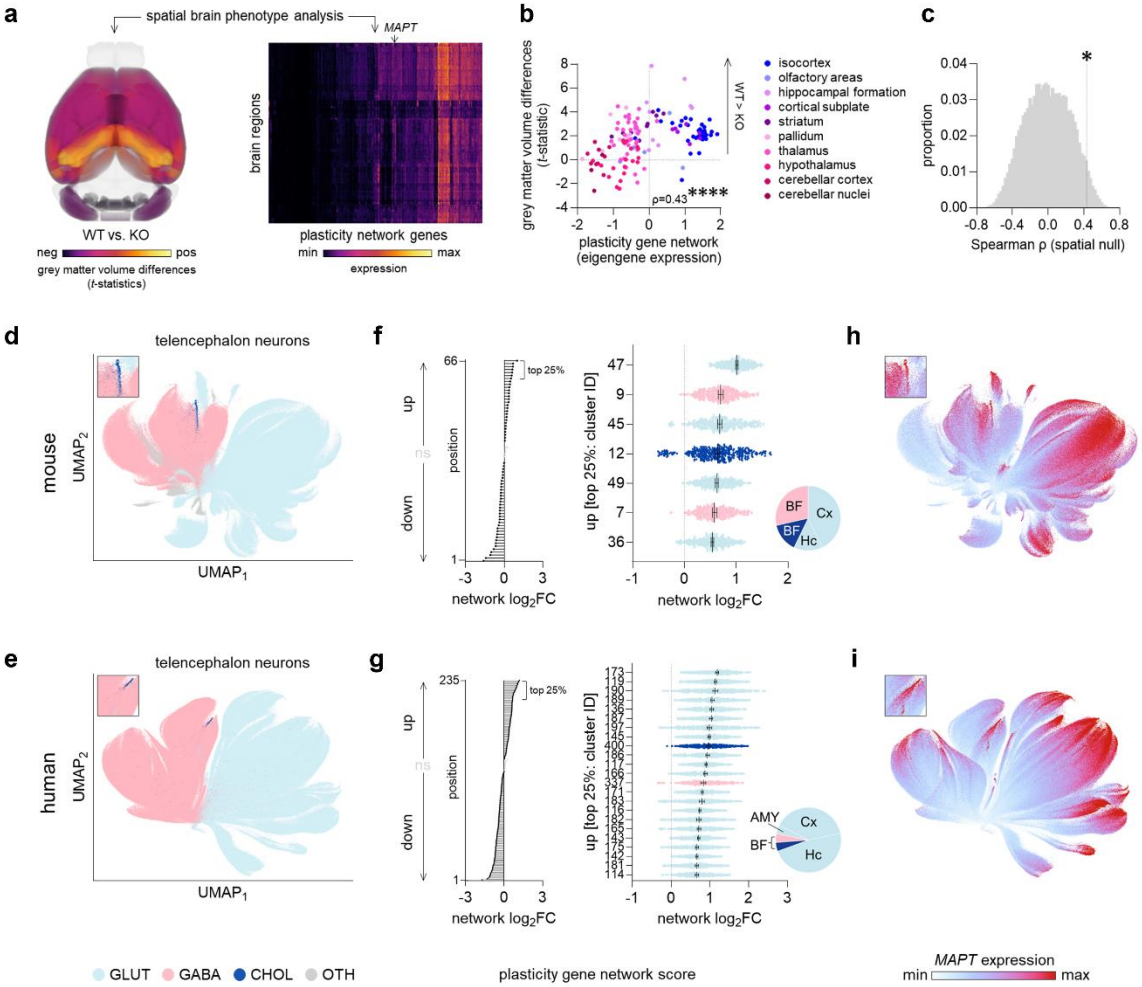

Fig. 4 Plasticity and vulnerability converge in basal forebrain cholinergic neurons and cholinoreceptive targets.

a, Schematic of spatial brain phenotyping analysis: (*left*) regional grey matter volume differences (*t*-statistics; neg-pos: -3–8) between VAChT KO and WT mice across parcels from the Allen Mouse Brian Atlas[63]; (*right*) heatmap displaying normalized expression levels of plasticity network genes from Roussarie *et al.*[59] across parcels from the Allen Mouse Brian Atlas[63], ordered using hierarchical clustering (expression; min-max: 0–50). **b,** Scatter plot

showing the relationship between the spatial profile of grey matter volume differences in WT versus KO mice and the first principal component (eigengene) of plasticity network expression, colour coded according to each parcel's region of origin (two-sided Spearman rank correlation). **c,** Histogram showing the distribution of 40,000 surrogate null Spearman ρ correlations computed from spatially autocorrelated random maps. The dotted line marks the observed correlation. **d,e,** Uniform manifold approximation and projection (UMAP) embedding by plasticity gene-network expression in telencephalon neurons from the healthy adult mouse[61] (**d**) and human[62] (**e**) brain, colour-coded by major neurochemical class. See *Methods* for details on selected snRNAseq atlases. **f,g,** (*left*) Bar plots show the median of $\log_2$FC values for differentially expressed plasticity network genes[59] across neuronal clusters in the mouse (**f**) and human (**g**) telencephalon, positioned according to the sign and significance of their network score. (*right*) Scatter plots illustrate the top 25% of neuronal clusters with significant positive gene-network expression scores (mouse: n=7; human: n=23) (median±95%CI; two-sided one sample Wilcoxon signed-rank test, adjusted for the false-discovery rate (FDR) at 5%). Scatter plots are colour-coded according to the neurochemical annotation legend in (**d**,**e**). Pie charts show the distribution of the top 25% of neuronal clusters by major neurochemical class and suspected region of origin (AMY=amygdala, BF=basal forebrain, Cx=cortex, Hc=hippocampus). **h,i,** UMAP plots highlighting raw *MAPT* expression values for each neuronal nuclei in the telencephalon of mice (**h**, min-max: 0–18) and humans (**i**, min-max: 0–30) (two-sided Wilcoxon rank-sum test; FDR-adjusted at 5%). Statistical details in **Supplemental Information Table 1**. Example mouse data displayed using MRIcroGL: https://www.nitrc.org/projects/mricrogl. *P≦0.05, ****P≦0.0001, ns,not significant. Source Data in **Source Data** file.

Discussion

We demonstrate that homeostatic synaptic plasticity serves as a common mechanism through which BF cholinergic neurons both adapt and contribute to early tau dysregulation, increasing their vulnerability to disease. Under physiological conditions, VAChT regulates cholinergic synaptic output in response to local network activity, while a *MAPT*-associated gene-network supports the presynaptic structural and molecular adaptations required to sustain this plasticity. Among the at-risk older adults studied here, our identification of both resilient and vulnerable subgroups suggests that there are distinct profiles of cholinergic synaptic adaptation to tau pathology in the aging brain. In resilient individuals, tau-induced synaptotoxicity was partially mitigated by a robust presynaptic VAChT response. In vulnerable individuals, a reduced capacity to mount this adaptive response was associated with tau propagation and cognitive decline.

The fundamental relationship between cholinergic presynaptic function and tau aligns with theoretical models of homeostatic synaptic plasticity[8–11,64], which posit that neurons adaptively regulate synaptic efficacy to preserve stability under sustained perturbation. Our data offers one of the first *in vivo* demonstrations of this mechanism in humans, wherein a graded presynaptic cholinergic response to tau pathology predicts long-term cognitive function and modulates tau spreading. Importantly, the failure of homeostatic synaptic plasticity in some individuals may explain the inflection point between normal brain aging and the AD trajectory. Such a progression echoes broader models of cellular aging, in which early transcriptomic, epigenetic, or metabolic disruptions trigger compensatory cellular adaptations that ultimately fail, leading to disease phenotypes[65].

Although we cannot exclude the contribution of soluble or intracellular Aβ to early changes in

cholinergic presynaptic function[66–71], particularly during the initial stages of AD, the insoluble Aβ pathology quantified by Aβ-PET[72] in this study did not colocalize with adaptive VAChT upregulation. Recent studies combining tau- and Aβ-PET imaging with cortical gene expression profiles[73,74] have shown that these proteinopathies propagate along distinct transcriptional pathways, with tau propagation aligning to axon-related genes, including *MAPT*, and Aβ propagation associating with dendrite-related profiles. These findings, together with our observations, suggest that while Aβ-related mechanisms may contribute to early neuronal dysfunction, the transcriptional programs governing tau-mediated cholinergic presynaptic adaptation and vulnerability operate through at least partially independent pathways.

Our findings in forebrain VAChT KO mice demonstrate causal interrelationships among cholinergic signalling, synaptic plasticity and the structural integrity of the BFpz. When the dynamic range of cholinergic neurotransmission is chronically constrained[75], as in VAChT KO mice, plasticity-dependent reversal learning is impaired. These deficits are partially rescued by enhancing acetylcholine availability, further underscoring the functional dependence of cognitive flexibility on cholinergic synaptic plasticity[54–56]. Forebrain VAChT KO mice also exhibited reductions in grey matter volume in brain regions densely innervated by BF cholinergic projections, including the hippocampus. We found that this profile of neurodegeneration spatially covaried with regional enrichment for *MAPT* and its associated gene-network supporting plasticity[59] in the healthy adult mouse brain. Deprivation of VAChT in cholinergic synapses may therefore disrupt cholinergic surveillance of transcriptional programs involved in plasticity, including tau proteostasis, initiating a cascade of cellular dysfunctions resembling early AD pathology[27,53].

Although *MAPT* is traditionally associated with microtubule stabilization, it exhibits strong co-expression with genes involved in presynaptic plasticity, vesicular transport, and neurotransmitter release[59,76,77]. Complementary experimental evidence suggests that one of the primary loci of tau pathology is in presynaptic terminals[78,79], where its mislocalization disrupts axonal transport, neurotransmitter release probability, and vesicle recycling through aberrant interactions with synaptic proteins and trafficking complexes. These dysfunctions are exacerbated by the unique morphofunctional properties of vulnerable neurons, including highly branched, lightly myelinated axons[80], and a sustained propensity for activity-dependent remodelling in adulthood[81]. Using snRNAseq atlases to survey neurons in the healthy adult mouse[61] and human[62] telencephalon, we show that *MAPT* and its associated plasticity gene-network are highly enriched in specific types of neurons which populate vulnerable brain regions, including BF cholinergic and GABAergic neurons and glutamatergic projection neurons of the hippocampus, cortex and amygdala. Together, our findings support the hypothesis that intrinsic, plasticity-linked transcriptional profiles predispose specific neuron types to early tau dysregulation[81–85]. Consistent with this idea, prior neuropathological work has shown that tau neurofibrillary tangles are present in virtually all older adults' brains by the age of 60[17,86], and tend to colocalize areas densely innervated by BF cholinergic projections[81,83,87].

The mechanistic link between VAChT and tau helps articulate new directions for future research. Do adaptive presynaptic responses to AD pathology exist in other neuronal populations? Why do these responses fail in some before others? Can this mechanism be modulated? Answers to these questions may inform therapeutic strategies that complement or preclude monoclonal antibodies targeting Aβ or tau[88].

Methods

Human Ethics Statement

All participants provided written informed consent at baseline (BL) and all follow-up (FL-U) visits. The consent forms along with study protocols for the data acquisition procedures (i.e., imaging, neuropsychological testing) were approved by the Institutional Review Board at McGill University and the CIUSSS de l'Ouest de l'Ile de Montréal Research Ethics Board (Montreal, QC, Canada).

Participants

Participants (n=64) were recruited from the PREVENT-AD program. A detailed description of the PREVENT-AD initiative and specific inclusion/exclusion criteria for participant recruitment and enrollment can be found in Tremblay-Mercier *et al.*[33]. PREVENT-AD is an ongoing, longitudinal observational study of older adults with a first-degree family history of AD (i.e., parental or multiple-siblings). At the time of enrollment, participants (≥55 years old) were screened to rule-out cognitive impairment using the Clinical Dementia Rating (CDR) scale and the Montreal Cognitive Assessment (MoCA) test. Information on participants' biological sex, number of years of education, and *APOE* genotype were collected at BL.

RBANS and Longitudinal Cognition Scores

All participants completed RBANS testing at BL and FL-U visits[89]. The RBANS includes 12 subtests (i.e., list learning, story learning, figure copy, line orientation, picture naming, semantic fluency, digit span, coding, list recall, list recognition, story recall, and figure recall)

which generate five index scores (i.e., immediate memory, delayed memory, language, attention, and visuospatial abilities) along with a total score. To minimize practice effects in longitudinal assessments, the battery was administered in four equivalent versions across visits.

Individual longitudinal changes in RBANS performance were quantified using the following formula:

$$\mathrm{APC} = \left[\left(\frac{\text{FL-U}}{\mathrm{BL}} \right)^{\frac{365}{\Delta \mathrm{DAYS}}} \text{-1} \right] \times 100$$

where ΔDAYS is given by the number of days between the most recent FL-U and BL visits of cognitive testing. APC was used to account for inter-individual differences in the time interval between BL and most recent FL-U visits (**Extended Data Fig. 1a**), as well as to investigate the relative change in RBANS total scores each year for every participant [90].

To compute adjusted RBANS APC total scores, a linear regression model with age at FL-U, BL RBANS total score, and years of education were entered as predictors of RBANS APC total score values. Gaussian Mixture Modelling (GMM) was then performed on the residual RBANS APC total scores. A two-component GMM was fitted using maximum likelihood estimation with a high iteration limit (maximum iterations = 10000) and multiple random starts (*n*=50) to ensure robust convergence. This yielded a two-cluster solution, with the primary separation occurring near a residual RBANS APC total score threshold of approximately -1% per year. We also replicated this two-cluster solution in a larger, out of sample cohort of PREVENT-AD participants (*n*=285).

Human Imaging Timeline

A summary of the human imaging data timeline is depicted in **Extended Data Fig. 1**. Structural MRI (sMRI) brain images were acquired starting from each participant's BL visit (2012-2017), up to and including their most recent FL-U visit (2018-2023). Participants returned for VAChT-PET ([^{18}F]-FEOBV) imaging within ~1 year of their most recent FL-U sMRI scan. Due to the nature of the COVID-19 pandemic, FL-U timepoint sMRI data for 11 participants were acquired ~1.5-2 years after their VAChT-PET scan. VAChT-PET scans were acquired within ~1.5 years of each participant's Tau-PET ([^{18}F]-AV1451) and Aβ-PET ([^{18}F]-NAV) scans (**Table 1**).

Human MRI Scanner Hardware and sMRI Data Acquisition

sMRI data acquisition took place at the Cerebral Imaging Center of the Douglas Mental Health University Institute Research Centre (Montreal, QC, Canada) between 2012-2023 (**Extended Data Fig. 1b**). For all participants, BL sMRI brain images from 2012 to 2017 were performed on a Siemens MAGNETOM 3T Tim Trio system. Starting in 2018, sMRI data were collected on an upgraded version of the same system (Siemens MAGNETOM 3T Prisma Fit). Both hardware (i.e., gradient, radiofrequency (RF), shimming) and software components of the system were included in this upgrade.

For sMRI data collected on the Siemens MAGNETOM 3T Tim Trio system, T1-weighted (T1w) images were acquired with a 3D magnetization prepared rapid gradient echo (MP-RAGE) sequence with the following parameters: matrix dimensions = 256 x 240 x 176; voxel size = 1 mm x 1 mm x 1 mm; repetition time (TR) = 2300 ms; echo time (TE) = 2.98 ms; inversion time (TI) = 900 ms; flip angle (FA) = 9˚; phase encode = anterior-posterior (A>>P); Bandwidth (BW) = 240 Hertz/pixel; GeneRalized Autocalibrating Partially Parallel

Acquisitions (GRAPPA) 2; acquisition time (TA) = 5.12 min. For sMRI data collected on the upgraded system (Siemens MAGNETOM 3T Prisma Fit), T1w images were acquired with a 3D MP-RAGE sequence encoding similar parameters: matrix dimensions = 256 x 256 x 192; voxel size = 1 mm x 1 mm x 1 mm; TR = 2300 ms; TE = 2.96 ms; TI = 900 ms; FA = 9°; phase encode = A>>P; BW = 240 Hertz/pixel; slice thickness = 1 mm; GRAPPA 2; TA = 5.30 min.

Longitudinal sMRI Data Processing

Preprocessing of human sMRI data was performed using the SPM12 toolbox (https://www.fil.ion.ucl.ac.uk/spm/software/spm12/) in MATLAB 2021b. A two-step method for longitudinal registration was implemented using the *serial longitudinal pipeline* from the SPM12 toolbox[91], as described previously[90,92]. First, the number of T1w scans acquired for each participant was determined. In the case of multiple T1w images within a single time point, the serial longitudinal pipeline was used to create an *intra-scan* average of the corresponding images. Next, an *inter-scan* midpoint average image from the collection of single or averaged T1w images was computed for each participant. The midpoint average T1w images were then segmented with the Computational Anatomy Toolbox's (CAT12[93]) *segmentation* module using tissue priors enhanced to improve the classification of subcortical grey matter[94]. The imported grey and white matter segments from the midpoint average T1w images were used to create a custom, age-appropriate cohort template by implementing diffeomorphic registration using geodesic shooting[95]. A deformation field between the cohort-specific template and each participant's midpoint average T1w image was also estimated during this step and then applied without modulation to the midpoint average T1w images to warp them into the cohort-specific template space. To ensure the integrity of all midpoint average T1w images for intermodal coregistration, a weighted-average Image Quality Rating (IQR) score was computed in CAT12[93]. Images with a CAT12 IQR below 70% were flagged for manual inspection. Finally,

the cohort-specific template was nonlinearly registered to the Human Connectome Project Multi-Modal Parcellation-extended (HCP MMPex) atlas space[49].

Human PET Radiotracer Synthesis

Radiotracer synthesis for human PET imaging took place on each scan date in the McConnell Brain Imaging Center's (BIC) Cyclotron Facility at McGill University (Montreal, QC, Canada). [^{18}F]-FEOBV was synthesized using a pure *levo* precursor (ABX advanced biochemical compounds, Radberg, DE) to obtain the (−)-FEOBV enantiomer, which is the only stereochemical configuration that exhibits binding affinity to VAChT[96]. ^{18}F labeling of (−)-FEOBV was performed in accordance with a previous study at the same site[20]. [^{18}F]-NAV4694 (Navidea Biopharmaceuticals, Dublin, OH) and [^{18}F]-AV1451 (Eli Lilly & Co, Indianapolis, IN) were synthesized and labelled in the same facility as previously described[97].

Human PET Scanner Hardware and Data Acquisition

All PET imaging took place in the BIC PET unit (Montreal, QC, Canada) on an ECAT High Resolution Research Tomograph (HRRT, CTI/Siemens) PET scanner. Prior to each participant's PET scans, a time-standardized transmission scan was acquired. For all participants, [^{18}F]-FEOBV brain PET imaging was conducted across two 30-minute imaging sessions, performed with a timing window of 6 ns and a 400–650 keV discrimination energy range[98]. The first session began following the intravenous injection of [^{18}F]-FEOBV and continued for 30 minutes (0–30 minutes; data not used in this study). Participants were then removed from the scanner before undergoing a second imaging session. This second session consisted of a 30-minute PET scan (180–210 minutes post-injection; 6 frames; 5 minutes/frame), corresponding to the established time period for [^{18}F]-FEOBV data acquisition in AD patients[20]. [^{18}F]-NAV4694 and [^{18}F]-AV1451 PET scans were acquired 40–70 minutes

(6 frames; 5 minutes/frame) and 80–100 minutes (4 frames; 5 minutes/frame) post-injection, respectively. All PET images were reconstructed using an iterative, 3D ordered subset expectation maximization (OSEM3D) algorithm with 10 iterations and 16 subsets and included corrections for 3D scattering[99]. Each frame was reconstructed to a final dimension of 256 x 256 x 207 and a voxel size of 1.22 mm x 1.22 mm x 1.22 mm.

Human PET Data Processing

Human VAChT ([^{18}F]-FEOBV), tau ([^{18}F]-AV1451) and Aβ ([^{18}F]-NAV) brain PET data were processed using the SPM12 toolbox (https://www.fil.ion.ucl.ac.uk/spm/software/spm12/) in MATLAB 2021b, as described previously[90,92]. Briefly, images were visually inspected to ensure proper orientation and centered to the anterior commissure. For each participant, an *intra-tracer* average of frames was computed, and the average images were coregistered to the corresponding native space midpoint average T1w image. The coregistered average PET images were then normalized to each participant's mean uptake within previously validated tracer-dependent reference regions (VAChT: supratentorial-supraventricular white matter[20,100]; Aβ: cerebellar grey matter[97]; tau: inferior cerebellar grey matter[97]) to produce SUVr images. The deformation fields created during the custom sMRI template building were used to warp the images without modulation into the cohort-specific template space.

Normative Deviation Mapping

To characterize participant-specific variations in tracer uptake, a normative deviation technique was adapted from prior work[41,42]. This method involves two key steps: (1) the computation of population median and deviation reference images and (2) the segmentation of individual voxel-wise data into discrete regions of interest (ROI).

Reference Image Computation: To compute reference images, the preprocessed PET data for each participant was taken as input. Given the age-range and unequal proportion of males and females in the cohort (**Table 1**), a general linear model with age and sex as covariates was used to adjust each individual's preprocessed PET images for these sources of variation. Additional preprocessing steps performed for normative deviation mapping included masking the PET data by a BFpz ROI. The BFpz ROI was created by combining the HCP MMPex[49] atlas parcels for all cortical, hippocampal, amygdalar, and BF regions into a binary mask, non-linearly warping this mask to the respective population template space and taking the logical overlap of this mask with the population template grey matter segmentation. The masked PET data were then smoothed using a 2 mm full-width at half-maximum (FWHM) Gaussian kernel.

For each tracer, reference images were separately generated in a leave-one-out cross-validation framework. Voxel-wise group medians were calculated across all participants, excluding the individual being processed in the current iteration to ensure independence:

$$\text{M-i} = \text{median}(\text{n-i})$$

where *i* is the participant being processed, *n-i* is the set of PET data excluding the left-out participant, and *M-i* is the resulting reference median image excluding the left-out participant.

Robust variability estimates were computed using the median absolute deviation (MAD). The MAD is computed as the median of the absolute deviations from the reference median image:

$$\text{MAD-i} = \text{median}(|(\text{n-i}) - (\text{M-i})|)\times\text{S}$$

where *MAD-i* is the resulting reference MAD image excluding the left-out participant. For normally distributed data, the MAD systematically underestimates the standard deviation. To correct for this, a scaling factor (*S*) of ~1.4826 was applied to the MAD, making it a consistent estimator of the standard deviation under the assumption of normality[101]. Finally, for each participant, both the *M-i* and *MAD-i* reference images were stored as 3D-volumetric images.

CI-Based Voxel Segmentation: Using the reference images (*M-i* and scaled *MAD-i*), each participant's PET data were segmented into four non-overlapping ROIs based on voxel-wise deviations from the reference images. The median deviation ROIs are: (1) below the lower 95% CI (<L95), (2) between the lower 95% CI and median (L95–M), (3) between the median and upper 95% CI (M–U95), and (4) above the upper 95% CI (>U95), given by the following equations:

I. $<\text{L95}: \text{i} < ((\text{M-i}) - (1.96 \times \text{MAD-i}))$

II. $\text{L95-M}: ((\text{M-i}) - (1.96 \times \text{MAD-i})) < \text{i} < (\text{M-i})$

III. $\text{M-U95}: (\text{M-i}) < \text{i} < ((\text{M-i}) + (1.96 \times \text{MAD-i}))$

IV. $>\text{U95}: \text{i} > ((\text{M-i}) + (1.96 \times \text{MAD-i}))$

For each segmentation step, continuous and binarized voxel masks were generated. Continuous maps retained the original voxel intensities, while binarized maps indicated voxel inclusion/exclusion. All SUVr extractions from normative deviation ROIs were performed using the binarized maps on the unsmoothed, adjusted PET images.

Reference Image Stability Analysis

To assess the stability of the population reference images (*M-i* or *MAD-i*) and independence

from individuals characterized by strong deviations from the rest of the population, correlations were performed for each pair of the computed *M-i* or *MAD-i* maps. This led to a distribution of Pearson *r* and Spearman ρ correlation coefficients based on (n x n-1)/2 = 2016 comparisons, given n=64 individuals.

Voxel-Wise Regressions of Human Multi-Tracer PET Data

To perform within-participant voxel-wise regressions, PET images for VAChT, tau, and Aβ were first masked using the binary anatomical BFpz image. Voxel values within the mask were then extracted, converted to vectors, and independently z-scored for each tracer, resulting in a normalized distribution of radiotracer uptake values for each participant. Linear regressions were then conducted using the voxel vectors for each individual:

I. $\mathrm{VAChT_v} = \beta 0_{\mathrm{indiv}} + \beta 1_{\mathrm{indiv}} \cdot \mathrm{Tau_v} + \beta 2_{\mathrm{indiv}} \cdot \mathrm{A\beta_v} + \varepsilon_{\mathrm{v}}$

II. $\mathrm{A\beta_v} = \beta 0_{\mathrm{indiv}} + \beta 1_{\mathrm{indiv}} \cdot \mathrm{Tau_v} + \beta 2_{\mathrm{indiv}} \cdot \mathrm{VAChT_v} + \varepsilon_{\mathrm{v}}$

where v is the voxel-wise maps, $\beta 0$ is the intercept, and ε is the unexplained variance.

Adaptive and Lag-Loss Spatial Overlap Models

To identify regions where VAChT is disproportionately high or low relative to tau, Jaccard index values were computed using each individual's VAChT and tau normative deviation mapping ROIs (<L95, <L95-M, >M-U95, >U95; referred to as $\mathrm{ROI_1}$-$\mathrm{ROI_4}$ below). Under the hypothesis that spatial patterns of co-localization may vary between resilient and vulnerable subgroups, two biologically motivated models of spatial overlap were computed: an *adaptive model*, in which VAChT exceeds tau by one deviation level (i.e., Tau-$\mathrm{ROI_1}$<VAChT-$\mathrm{ROI_2}$, Tau-$\mathrm{ROI_2}$<VAChT-$\mathrm{ROI_3}$, Tau-$\mathrm{ROI_3}$<VAChT-$\mathrm{ROI_4}$), and a *lag-loss model*, in which tau

exceeds VAChT by one deviation level (i.e., VAChT-ROI_1<Tau-ROI_2, VAChT-ROI_2<Tau-ROI_3, VAChT-ROI_3<Tau-ROI_4). Note that voxels indexed by the adaptive and lag-loss models are spatially independent of one another. For both models, the Jaccard index values for its constituent ROI pairs were averaged to produce a model summary statistic for each individual. To determine the spatial expression of the models in resilient and vulnerable subgroups, a voxel-wise conjunction map of each model's ROI pairs was generated for all participants. For each map, the percent overlap with BFpz parcels from the HCP MMPex atlas[49] was computed.

Mouse Ethics Statement

All small-animal imaging procedures were conducted in accordance with the Canadian Council of Animal Care's current policies and were approved by the University of Western Ontario's Animal Care Committee (Animal Use Protocols: 2020-163) and the Lawson Health Research Institute's Health and Safety board. Mice were housed as pairs in standard plexiglass cages in temperature- and humidity-controlled rooms (22–25˚C, 40%–60%) on 12-hour light/12-hour dark cycles, where food (regular chow) and water were made available *ad libitum*. Imaging and touchscreen experiments were performed during the light cycle (7:00 AM–7:00 PM). All efforts were made to maximize animal welfare before, during, and after experiments.

Mouse Multimodal Imaging Experimental Overview

High-resolution *in vivo* 9.4 T sMRI and [^{18}F]-FEOBV microPET data were acquired at the Center of Functional and Metabolic Mapping (Agilent Animal MRI Scanner, Bruker) and the Lawson Health Research Institute's Preclinical Imaging Facility (Inveon DPET, Siemens Healthineers), respectively. All imaging data were acquired in mice at 6–7 months of age. Data were acquired in WT mice (WT: MRI = 8 male, 6 female; PET = 5 male, 6 female), either C57BL/6 J or VAChT$^{flox/flox}$, VAChT$^{Nk2x.1\text{-}Cre\text{-}flox/flox}$ mice (KO: MRI = 5 male, 5 female; PET

= 4 male, 3 female), Nkx2.1-Cre mice (CRE: MRI = 3 male, 3 female), and ChAT-ChR2-eYFP mice (HYP: MRI/PET = 4 male, 3 female). A different analysis of the [^{18}F]-FEOBV microPET data for the WT mice (*n*=11) can be found in the reporting laboratories' previously published study[102]. VAChT$^{flox/flox}$ and VAChT$^{Nk2x.1\text{-}Cre\text{-}flox/flox}$ mice were generated on a C57BL/6 J background as previously described[27,103]. Nkx2.1-Cre (C57BL/6J-Tg(Nkx2-1-cre)2Sand/J) and ChAT-ChR2-eYFP mice (B6.Cg-Tg(Chat-COP4*H134R/EYFP)6Gfng/J) were purchased from The Jackson Laboratory (JAX: stock no. 008661, stock no. 014546), with the latter maintained as hemizygous.

Mouse sMRI Data Acquisition

Mice were anesthetized with 1.5–2.0% isoflurane in 1.5 L min^{-1} O_2 (g) and then moved to the center of a 30 mm RF volume coil (Bruker). Four iterations of 3D magnetization transfer (MT)-weighted spoiled gradient-recalled echo (GRE) images were acquired using a fast low-angle shot pulse sequence with the following parameters: FOV = 16 mm x 16 mm x 10 mm; matrix dimensions = 128 x 128 x 8; voxel size = 0.125 mm x 0.125 mm x 0.125 mm, slice thickness = 10 µm; TR = 30 ms; TE = 2.77 ms; FA = 9°; off-resonance saturation = 4.5 kHz (Gaussian pulse = 10 ms duration); effective FA = 900°[104].

Mouse sMRI Data Processing

Preprocessing of mouse anatomical brain images was performed using the SPM12 toolbox (https://www.fil.ion.ucl.ac.uk/spm/software/spm12/) in MATLAB 2020b as described previously[102]. Anatomical images (*n*=4) were averaged, resized, centered, and re-oriented to follow the right-hand coordinate system (RAS). Images were then coregistered to the mouse brain template from Hikishima *et al.*[105], bias-corrected using MICO[106], and segmented using tissue priors for grey matter, white matter, and cerebrospinal fluid tissue compartments[105]. The

grey and white matter segmentations were then used to create nonlinear transformations for diffeomorphic registration to a study-specific average template using geodesic shooting[95]. Finally, the deformation fields estimated during the template-building step were applied with modulation to each mouse's grey matter segment to warp the images to template space. To parcellate mouse anatomical (and [^{18}F]-FEOBV, see below) brain images, the study-specific mouse brain template was non-linearly registered to the Allen Mouse Brain Atlas (ABA) common coordinate framework version 3 (ABAccfv3)[57]. For WT, KO, and CRE mice, brain regions for grey matter volume extractions were defined according to the symmetrized, coarse annotated ABAccfv3[57]. Extractions were restricted to voxels within each mouse's grey matter tissue segment that had a probability of at least 0.1 of belonging to the grey matter. Grey matter volume extractions were performed on the unsmoothed, modulated-warped grey matter segments, adjusted for each mouse's total intracranial volume (TIV), which was calculated by summing the grey matter, white matter and cerebrospinal fluid volumes in the *seg8.mat file created during segmentation[107].

Mouse [^{18}F]-FEOBV microPET Data Acquisition

In vivo, dynamic [^{18}F]-FEOBV microPET data were acquired in WT, KO, and HYP mice, as previously described[102]. All [^{18}F]-FEOBV microPET imaging sessions were performed as 150-minute list-mode emission scans, with a timing window of 3.432 ns and a 350–640 keV discrimination energy range. Mice were anesthetized with 1.5–2.0% isoflurane in 1.0 L min^{-1} O_2 (g) and then injected intravenously with ~20 Megabecquerel (MBq) of [^{18}F]-FEOBV. Data were binned into 15 frames of 40 seconds, followed by 28 frames of 300 seconds. An OSEM3D algorithm with two iterations and 18 subsets was used to reconstruct [^{18}F]-FEOBV microPET images with the following parameters: matrix dimensions: 128 × 128 × 159; voxel size: 0.776 mm × 0.776 mm × 0.796 mm.

Mouse [^{18}F]-FEOBV microPET Data Processing

Parametric total volume of distribution (V_T) images for each mouse's [^{18}F]-FEOBV data were estimated as described previously[102]. Whole-brain [^{18}F]-FEOBV time-activity curves were fit according to Logan *et al.*[108], where an image-derived input function (IDIF) from the lumen of the left ventricle of the heart served as the reference[102]. Preprocessing of mouse [^{18}F]-FEOBV V_T images was performed using the SPM12 toolbox (https://www.fil.ion.ucl.ac.uk/spm/software/spm12/) in MATLAB 2020b. Preparation of [^{18}F]-FEOBV V_T images included resizing, centering, and re-orienting the images to follow the RAS. Each V_T image was then coregistered and cropped to the bounding box of its corresponding native space MRI image, and warped without modulation to the study-specific anatomical mouse brain template. For WT and HYP mice, extractions of average [^{18}F]-FEOBV uptake in the mouse BFpz, hippocampus and cortex were performed using region-specific masks based on the ABAccfv3[57]. A similar approach was also taken to create masks for extracting average [^{18}F]-FEOBV uptake in the forebrain (BFpz and striatum) and brainstem (midbrain, pons, and medulla) of WT and KO mice. In all cases, average uptake was calculated on the unsmoothed, warped [^{18}F]-FEOBV V_T brain images.

Western Blotting

Brain tissue samples for Western blotting were collected in a subset of WT, HYP, and KO mice following [^{18}F]-FEOBV microPET scans. Mice were anesthetized via intraperitoneal injection of a ketamine (100 mg kg^{-1}) - xylazine (25 mg kg^{-1}) 0.9% sodium chloride solution and then euthanized by cervical dislocation. Brain tissue was extracted, rapidly dissected on ice into appropriate tissue compartments (i.e., brainstem, striatum, hippocampus, cortex), snap-frozen on liquid nitrogen, and stored in 2 mL microcentrifuge tubes at -80˚C until needed. Protein

isolation and immunoblotting were performed as previously described[109]. Briefly, tissue samples were thawed on ice and homogenized in RIPA buffer (50 mM Tris, 150 mM NaCl, 0.1% SDS, 0.5% sodium deoxycholate, 1% triton X-100, pH 8.0), supplemented with phosphatase inhibitors (1 mM NaF and 0.1 mM Na_3VO_4) and a protease inhibitor cocktail (diluted 1:100, Cat#539134-1SET; Calbiochem). Homogenates were sonicated, rocked for 20 minutes at 4˚C, and then centrifuged at 10,000g for 20 minutes at 4˚C. Supernatants were collected and protein quantification was performed using the Pierce™ BCA Protein Assay Kit (Cat#23227; ThermoFisher Scientific). 20–25 µg of protein were loaded and separated on 4–12% Bis-Tris Protein Gels (Cat#NW04125BOX; Invitrogen) and then transferred onto PVDF membranes (Cat#IPVH00010; EMD Millipore) using the Trans-Blot Turbo system (Bio-Rad Laboratories, Hercules, CA, USA). Membranes were blocked for 60 minutes in 5% milk (for VAChT) or 5% BSA (for Synaptophysin) in 1xTBST. Primary antibodies included rabbit anti-VAChT (diluted 1:2000, Cat#139103; Synaptic Systems) and mouse anti-Synaptophysin (diluted 1:2000, Cat#ab8049; Abcam). Following 4˚C overnight primary antibody incubation in the respective blocking solutions, membranes were washed and then incubated for 60 minutes at room temperature in corresponding horseradish peroxidase (HRP)-conjugated secondary antibodies. Bands were visualized using enhanced chemiluminescence (ECL) detection reagents in a ChemiDoc Imaging System (Bio-Rad Laboratories, Hercules, CA, USA). Densitometric analysis was performed in ImageLab (Bio-Rad Laboratories, Hercules, CA, USA).

PVD-PVR Touchscreen Testing

7 month-old WT (*n*=6) and KO (*n*=19) mice (male) were tested on the PVD-PVR task (SOP2; www.touchscreencognition.org) developed for the rodent automated Bussey-Saksida Touchscreen System (Model 81426, Campden Instruments, Lafayette, Indiana) with Abet II

Touch Software Version 2.20 (Lafayette Instrument Company, Lafayette, Indiana). PVD-PVR is designed to measure the effects of pharmacological or genetic manipulation on visual learning and cognitive flexibility[110]. Prior to PVD-PVR testing, all mice completed behavioural habituation, pre-training stages and acquisition sessions in the touchscreen chamber[111]. Following meeting acquisition criteria, mice were subject to PVD. PVD requires mice to learn to associate a food reward (7 µL strawberry milkshake) with a nose-poke response to a correct image (S^+ stimulus) in one touchscreen window, while simultaneously ignoring a second visually-distinct, incorrect image (S^- stimulus) in the other touchscreen window. After completing six PVD sessions (two pre-pump implantation, four post-pump implantation), mice were tested on PVR learning across 10 sessions. In PVR, the strawberry milkshake food reward becomes linked to the previously incorrect image (S^- stimulus), while nose poke responses to the former correct image (S^+ stimulus) are no longer reinforced.

Subcutaneous Osmotic Pump Implantation and Pharmacological Manipulation Paradigm

During PVD-PVR testing, a subset of KO mice underwent pharmacological manipulation by the continuous administration of the acetylcholinesterase inhibitor, donepezil, via subcutaneous osmotic pumps. Donepezil hydrochloride (C6821-50mg) monohydrate was obtained from Sigma-Aldrich (Oakville, Ontario) and rehydrated using saline and 10% dimethyl sulfoxide (DMSO) to a dose of 1.5 mg kg^{-1}. Dosage was determined using the Alzet drug concentration calculator to account for pump model and corresponding flow rate as well as the weight of the mice. Implantation of subcutaneous osmotic pumps (model 1004, Alzet, Durect Corporation, Cupertino, California) was performed in WT and KO mice following completion of PVD session two. Pumps were designed to deliver continuous treatment (WT (n=6) or KO (n=8): saline + 10% DMSO; KO (n=11): 1.5 mg kg^{-1} of donepezil) at a fixed rate

of 0.11μL/hr for 28 days. Preparation for pump insertion included loading each pump with a 1 mL syringe, capping the pumps with a pin, and soaking them in saline with <1 hour to implantation. Prior to pump insertion, mice were anesthetized with isoflurane (4%, initial; 1.5%, maintenance) in 1 L min^{-1} O_2 (g) and put in a recumbent prone position. A small incision was made in the upper-right quadrant of each mouse's back, followed by the insertion of a pump and sealing of the incision site with a wound clip. Mice were given two days to recover from the surgeries before beginning session three of PVD.

Spatial Brain Phenotype Analysis

Regional *t*-statistics representing grey matter volume differences between forebrain VAChT KO and WT mice were computed for 212 anatomical parcels from the ABA, based on the parcellation scheme from Oh *et al.*[63]. Parcels in the brainstem (i.e., midbrain, pons, medulla) and low-intensity olfactory bulb areas were excluded, yielding 144 parcels for analysis. Corresponding regional *in situ* hybridization (ISH) data were obtained from the ABA[58], preprocessed as described previously[60]. For each parcel, gene expression was represented as "energy" scores, reflecting expression levels weighted by hybridization intensity. To perform module based analyses, a gene-network enriched for presynaptic functions vulnerable to dysregulation in AD was obtained from Supplemental Table 5 in Roussarie *et al.*[59] ('Module C', *n*=702). Genes from this network that lacked expression data across an entire parcel were removed. After merging and cleaning, 401 of the 702 genes in the original module remained. A principal-component analysis was then applied to the cleaned gene-by-region matrix, and the first principal component was saved. The resulting eigengene score captured the dominant axis of co-expression within the plasticity gene module. Spearman rank correlation coefficients were computed between the region-wise profile of grey matter volume differences and the selected transcriptional profile (i.e., the module eigengene). To assess statistical significance

while accounting for spatial autocorrelation, the observed correlation was compared to a null distribution generated from 40,000 spatial surrogate maps[112,113]. These surrogate maps preserved the intrinsic spatial autocorrelation structure of gene expression but randomized regional assignments[60,113]. A one-tailed *P*-value was computed as the proportion of surrogate correlations greater than the observed correlation.

Whole-Brain snRNAseq Analysis

Whole-brain adult human (~3 million nuclei) and mouse (~6 million nuclei) snRNAseq atlases were downloaded from Siletti *et al.*[62] and Langlieb *et al.*[61], respectively. Metadata provided with each dataset were used to annotate clusters according to cell-type (i.e., neuron, glia) and developmental compartment (i.e., telencephalon, diencephalon, mesencephalon, rhombencephalon). Only clusters annotated as neuronal and telencephalic were used (mouse: n=66; human: n=235).

Cluster-wise Differential Expression Analysis: Gene-sets for each telencephalic neuron cluster were filtered to include only genes which had non-zero expression values in >25% of the cluster's representative nuclei[114]. For each gene in a cluster's filtered gene-set, the arithmetic mean of the gene's expression within the cluster was computed (target mean), as well as the arithmetic mean of its expression across all other clusters, excluding the target cluster (reference mean). The $\log_2$ fold-change ($\log_2$FC) value for each gene in a target-reference pair was then calculated using these means. Differential expression (DE) of genes was assessed between all target-reference pairs with two sample Wilcoxon rank-sum tests. To adjust for multiple testing across clusters, false-discovery rate (FDR)-correction (5% threshold) was applied to the raw *P*-values generated from the rank-sum tests using the Benjamini–Hochberg procedure.

Gene-Network Expression Analysis and Centrality: The plasticity gene-network list ('Module C') was obtained from Roussarie *et al.*[59]. For each cluster, the median and 95% CIs of the $\log_2$FC values for all DE genes (after FDR-adjustment) participating in the gene-network were computed. Median values were then ranked and filtered to the top 25% of clusters expressing significant positive median gene-network scores in the mouse (n=7) and human (n=23) datasets. To determine the genes central to the gene-network as expressed by BF cholinergic neurons in the adult mouse (MC_12) and human (SPLAT_400) brain, the significant edges from the functional graph in Roussarie *et al.*[59] were obtained. All edges within the graph were then reweighted by the expression level of the genes at either end of each edge in BF cholinergic neurons using the geometric mean:

$$W_{ij} = \sqrt[3]{p_{ij} * \hat{e}_i * \hat{e}_j}$$

where:

$$\hat{e}_i = \frac{e_i}{\max_{k \in M} e_k}$$

And p_{ij} is the posterior probability of an edge in the original network, M is the set of all genes in the gene-network, e_i is the expression of gene i in BF cholinergic neurons. For both mouse and human BF cholinergic neurons, only overlapping genes with positive $\log_2$FC values were included in centrality analyses. Degree centrality was calculated on the reweighted, undirected network as the sum of edges connected to each gene.

Statistical Analysis

Statistical analyses were conducted using GraphPad Prism (version 10.4.1; GraphPad Software, La Jolla, CA), except for robust regressions and imaging analyses which were performed in MATLAB 2021b, and spatial brain phenotyping and snRNAseq analyses, which were carried out in Python v3.13.2. Sample sizes were determined based on previous studies in the field. Parametric tests and their corresponding post hoc comparisons were applied to groups with a sample size of at least 10 that met assumptions of normality (Kolmogorov–Smirnov test for $n>50$ or Shapiro-Wilk test for $n<50$) and homoscedasticity (Bartlett test). When these assumptions were not met, non-parametric tests with appropriate post hoc analyses were used. Statistical test results are provided in the figure legends and **Supplemental Information** tables. All statistical analyses were performed at a $P_{crit}=0.05$, with adjustments for multiple comparisons or controlling for the FDR (5%), as needed.

Code and Data Availability

Human imaging and cognition data are from the PREVENT-AD program, which is promoting data access for the scientific community via their Canadian Alzheimer Platform (Brain Canada Foundation). For more information regarding PREVENT-AD data usage and availability, please refer to https://www.centre-stopad.com/en/plateforme-cap. The ABA ISH data[58] is publicly available for download (https://community.brain-map.org/t/in-situ-hybridization-ish-data/2762). The mouse[61] (https://docs.braincelldata.org/downloads) and human[62] (https://alleninstitute.github.io/abc_atlas_access/descriptions/WHB_dataset.html) snRNAseq atlases are publicly available for download. The list of genes used to compute plasticity gene-network scores ('Module C') can be found in Table S5 from Roussarie *et al.*[59]. All [^{18}F]-FEOBV microPET datasets will be made available for download upon publication of the manuscript. Mouse anatomical images are under active use by the reporting laboratories and

can be made available by contacting tschmitz@uwo.ca. All code will be made available upon publication of the manuscript. Source data for all figures are in the corresponding **Source Data** files.

Acknowledgements

Consortia

for the PREVENT-AD Research Group

J. Breitner, J. Poirier, S. Villeneuve, H. Zetterberg, K. Blennow, A. A. Baril, M. Geddes, S. Ducharme, M. Montembeault, R.N. Spreng, A. Pichet-Bessette, L. Munter, M. Tedeshi-Dauar, C. Picard, A. Labonté, G. Aumont-Rodrigue, J. Ao, I. Sarty, J. Loncke & A. Poirier

Corresponding Author

Correspondence to Taylor W. Schmitz: tschmitz@uwo.ca.

Ethics Declaration

Competing Interests

J.P. serves as a scientific advisor to the Alzheimer Foundation of France. T.J.B and L.M.S have established a series of targeted cognitive tests for animals, administered via touchscreen with a custom environment known as the Bussey-Saksida touchscreen chamber. Cambridge Enterprise, the technology transfer office of the University of Cambridge, supported commercialization of the Bussey-Saksida chamber, culminating in a license to Campden Instruments. Any financial compensation received from commercialization of the technology is fully invested in further touchscreen development and/or maintenance. All other authors declare no competing interests.

References

1. Davies, C. A., Mann, D. M. A., Sumpter, P. Q. & Yates, P. O. A quantitative morphometric analysis of the neuronal and synaptic content of the frontal and temporal cortex in patients with Alzheimer's disease. *J. Neurol. Sci.* **78**, 151–164 (1987).
2. Lleó, A. *et al.* Changes in synaptic proteins precede neurodegeneration markers in preclinical Alzheimer's disease cerebrospinal fluid. *Mol. Cell. Proteomics* **18**, 546–560 (2019).
3. DeKosky, S. T. & Scheff, S. W. Synapse loss in frontal cortex biopsies in Alzheimer's disease: correlation with cognitive severity. *Ann. Neurol.* **27**, 457–464 (1990).
4. Terry, R. D. *et al.* Physical basis of cognitive alterations in Alzheimer's disease: synapse loss is the major correlate of cognitive impairment. *Ann. Neurol.* **30**, 572–580 (1991).
5. Scheff, S. W., Price, D. A., Schmitt, F. A. & Mufson, E. J. Hippocampal synaptic loss in early Alzheimer's disease and mild cognitive impairment. *Neurobiol. Aging* **27**, 1372–1384 (2006).
6. Klein, W. L. Synaptic targeting by A beta oligomers (ADDLS) as a basis for memory loss in early Alzheimer's disease. *Alzheimers. Dement.* **2**, 43–55 (2006).
7. Chen, M.-K. *et al.* Assessing synaptic density in Alzheimer disease with synaptic vesicle glycoprotein 2A positron emission tomographic imaging. *JAMA Neurol.* **75**, 1215–1224 (2018).
8. Davis, G. W. Homeostatic control of neural activity: from phenomenology to molecular design. *Annu. Rev. Neurosci.* **29**, 307–323 (2006).
9. Marder, E. & Goaillard, J.-M. Variability, compensation and homeostasis in neuron and network function. *Nat. Rev. Neurosci.* **7**, 563–574 (2006).
10. Turrigiano, G. G. The self-tuning neuron: synaptic scaling of excitatory synapses. *Cell*

135, 422–435 (2008).

11. Pozo, K. & Goda, Y. Unraveling mechanisms of homeostatic synaptic plasticity. *Neuron* **66**, 337–351 (2010).
12. Jack, C. R., Jr *et al.* Prevalence of biologically vs clinically defined Alzheimer spectrum entities using the National Institute on aging-Alzheimer's Association research framework. *JAMA Neurol.* **76**, 1174–1183 (2019).
13. de Vries, L. E., Huitinga, I., Kessels, H. W., Swaab, D. F. & Verhaagen, J. The concept of resilience to Alzheimer's Disease: current definitions and cellular and molecular mechanisms. *Mol. Neurodegener.* **19**, 33 (2024).
14. Mesulam, M., Shaw, P., Mash, D. & Weintraub, S. Cholinergic nucleus basalis tauopathy emerges early in the aging-MCI-AD continuum. *Ann. Neurol.* **55**, 815–828 (2004).
15. Grothe, M., Heinsen, H. & Teipel, S. Longitudinal measures of cholinergic forebrain atrophy in the transition from healthy aging to Alzheimer's disease. *Neurobiol. Aging* **34**, 1210–1220 (2013).
16. Schmitz, T. W., The Alzheimer's Disease Neuroimaging Initiative & Nathan Spreng, R. Basal forebrain degeneration precedes and predicts the cortical spread of Alzheimer's pathology. *Nat. Commun.* **7**, 13249 (2016).
17. Braak, H., Thal, D. R., Ghebremedhin, E. & Del Tredici, K. Stages of the pathologic process in Alzheimer disease: age categories from 1 to 100 years. *J. Neuropathol. Exp. Neurol.* **70**, 960–969 (2011).
18. Schmitz, T. W. *et al.* Longitudinal Alzheimer's Degeneration Reflects the Spatial Topography of Cholinergic Basal Forebrain Projections. *Cell Rep.* **24**, 38–46 (2018).
19. Fernández-Cabello, S. et al. Basal forebrain volume reliably predicts the cortical spread of Alzheimer's degeneration. *Brain* **143**, 993–1009 (2020).
20. Aghourian, M., Legault-Denis, C. & Soucy, J. P. Quantification of brain cholinergic

denervation in Alzheimer's disease using PET imaging with [18 F]-FEOBV. *Mol Psychiatry* **22**, 1531–1538 (2017).

21. Kilgard, M. P. & Merzenich, M. M. Cortical map reorganization enabled by nucleus basalis activity. *Science* **279**, 1714–1718 (1998).
22. Ramanathan, D., Tuszynski, M. H. & Conner, J. M. The basal forebrain cholinergic system is required specifically for behaviorally mediated cortical map plasticity. *J. Neurosci.* **29**, 5992–6000 (2009).
23. Gu, Z. & Yakel, J. L. Timing-dependent septal cholinergic induction of dynamic hippocampal synaptic plasticity. *Neuron* **71**, 155–165 (2011).
24. Pinto, L. *et al.* Fast modulation of visual perception by basal forebrain cholinergic neurons. *Nat. Neurosci.* **16**, 1857–1863 (2013).
25. Froemke, R. C., Merzenich, M. M. & Schreiner, C. E. A synaptic memory trace for cortical receptive field plasticity. *Nature* **450**, 425–429 (2007).
26. Bakin, J. S. & Weinberger, N. M. Induction of a physiological memory in the cerebral cortex by stimulation of the nucleus basalis. *Proc. Natl. Acad. Sci. U. S. A.* **93**, 11219–11224 (1996).
27. Kolisnyk, B. *et al.* Cholinergic Surveillance over Hippocampal RNA Metabolism and Alzheimer's-Like Pathology. *Cereb. Cortex* **27**, 3553–3567 (2017).
28. Schmitz, T. W., Soreq, H., Poirier, J. & Spreng, R. N. Longitudinal basal forebrain degeneration interacts with TREM2/C3 biomarkers of inflammation in pre-symptomatic Alzheimer's disease. *J. Neurosci.* **40**, 1931–1942 (2020).
29. Hahm, E.-T., Nagaraja, R. Y., Waro, G. & Tsunoda, S. Cholinergic homeostatic synaptic plasticity drives the progression of Aβ-induced changes in neural activity. *Cell Rep.* **24**, 342–354 (2018).
30. Legault-Denis, C. *et al.* Parkinson's disease CA2-CA3 hippocampal atrophy is

accompanied by increased cholinergic innervation in patients with normal cognition but not in patients with mild cognitive impairment. *Brain Imaging Behav.* **18**, 783–793 (2024).

31. Ananth, M. R. *et al.* A central role for acetylcholine in entorhinal cortex function and dysfunction with age in humans and mice. *Cell Rep.* **44**, 115249 (2025).
32. Wu, D. *et al.* Targeting a vulnerable septum-hippocampus cholinergic circuit in a critical time window ameliorates tau-impaired memory consolidation. *Mol. Neurodegener.* **18**, 23 (2023).
33. Tremblay-Mercier, J. *et al.* Open science datasets from PREVENT-AD, a longitudinal cohort of pre-symptomatic Alzheimer's disease. *NeuroImage Clin.* **31**, 102733 (2021).
34. Mulholland, G. K. *et al.* [18F]fluoroethoxy-benzovesamicol, a PET radiotracer for the vesicular acetylcholine transporter and cholinergic synapses. *Synapse* **30**, 263–274 (1998).
35. Weihe, E., Tao-Cheng, J. H., Schäfer, M. K., Erickson, J. D. & Eiden, L. E. Visualization of the vesicular acetylcholine transporter in cholinergic nerve terminals and its targeting to a specific population of small synaptic vesicles. *Proc. Natl. Acad. Sci. U. S. A.* **93**, 3547–3552 (1996).
36. Prado, M. A. M. *et al.* Regulation of acetylcholine synthesis and storage. *Neurochem. Int.* **41**, 291–299 (2002).
37. Vogel, J. W. *et al.* Four distinct trajectories of tau deposition identified in Alzheimer's disease. *Nat. Med.* **27**, 871–881 (2021).
38. Collij, L. E. *et al.* Spatial-temporal patterns of β-amyloid accumulation: A subtype and Stage Inference model analysis. *Neurology* **98**, e1692–e1703 (2022).
39. Young, C. B. *et al.* Divergent cortical tau positron emission tomography patterns among patients with preclinical Alzheimer disease. *JAMA Neurol.* **79**, 592–603 (2022).

40. Murray, M. E. *et al.* Neuropathologically defined subtypes of Alzheimer's disease with distinct clinical characteristics: a retrospective study. *Lancet Neurol.* **10**, 785–796 (2011).

41. Chen, H. *et al.* Quantile rank maps: a new tool for understanding individual brain development. *Neuroimage* **111**, 454–463 (2015).

42. Bethlehem, R. A. I. *et al.* Brain charts for the human lifespan. *Nature* **604**, 525–533 (2022).

43. Wu, M. *et al.* The role of pathological tau in synaptic dysfunction in Alzheimer's diseases. *Transl. Neurodegener.* **10**, 45 (2021).

44. Busche, M. A. & Hyman, B. T. Synergy between amyloid-β and tau in Alzheimer's disease. *Nat. Neurosci.* **23**, 1183–1193 (2020).

45. Shankar, G. M. & Walsh, D. M. Alzheimer's disease: synaptic dysfunction and Abeta. *Mol. Neurodegener.* **4**, 48 (2009).

46. Ao, J. *et al.* Novel synaptic markers predict early tau pathology and cognitive deficit in an asymptomatic population at risk of Alzheimer's disease. *Mol. Psychiatry* **30**, 2810–2820 (2025).

47. Palmqvist, S. *et al.* Earliest accumulation of β-amyloid occurs within the default-mode network and concurrently affects brain connectivity. *Nat. Commun.* **8**, 1214 (2017).

48. Sanchez, J. S. *et al.* The cortical origin and initial spread of medial temporal tauopathy in Alzheimer's disease assessed with positron emission tomography. *Sci. Transl. Med.* **13**, eabc0655 (2021).

49. Huang, C.-C., Rolls, E. T., Feng, J. & Lin, C.-P. An extended Human Connectome Project multimodal parcellation atlas of the human cortex and subcortical areas. *Brain Struct. Funct.* **227**, 763–778 (2022).

50. Doering, S. *et al.* Deconstructing pathological tau by biological process in early stages of Alzheimer disease: a method for quantifying tau spatial spread in neuroimaging.

EBioMedicine **103**, 105080 (2024).

51. Ozlen, H. *et al.* Spatial extent of amyloid-β levels and associations with tau-PET and cognition. *JAMA Neurol.* **79**, 1025–1035 (2022).
52. Kolisnyk, B. *et al.* ChAT–ChR2–EYFP Mice Have Enhanced Motor Endurance But Show Deficits in Attention and Several Additional Cognitive Domains. *J. Neurosci.* **33**, 10427–10438 (2013).
53. Al-Onaizi, M. A. *et al.* Regulation of Cognitive Processing by Hippocampal Cholinergic Tone. *Cereb. Cortex* **27**, 1615–1628 (2017).
54. Kolisnyk, B. *et al.* Forebrain deletion of the vesicular acetylcholine transporter results in deficits in executive function, metabolic, and RNA splicing abnormalities in the prefrontal cortex. *J. Neurosci.* **33**, 14908–14920 (2013).
55. Ridley, R. M., Baker, J. A., Baker, H. F. & Maclean, C. J. Restoration of cognitive abilities by cholinergic grafts in cortex of monkeys with lesions of the basal nucleus of Meynert. *Neuroscience* **63**, 653–666 (1994).
56. Cabrera, S. M., Chavez, C. M., Corley, S. R., Kitto, M. R. & Butt, A. E. Selective lesions of the nucleus basalis magnocellularis impair cognitive flexibility. *Behav. Neurosci.* **120**, 298–306 (2006).
57. Wang, Q. *et al.* The Allen Mouse Brain Common Coordinate Framework: A 3D Reference Atlas. *Cell* **181**, 936–953.e20 (2020).
58. Lein, E. S. *et al.* Genome-wide atlas of gene expression in the adult mouse brain. *Nature* **445**, 168–176 (2007).
59. Roussarie, J.-P. *et al.* Selective neuronal vulnerability in Alzheimer's disease: A network-based analysis. *Neuron* **107**, 821–835.e12 (2020).
60. Fulcher, B. D., Arnatkeviciute, A. & Fornito, A. Overcoming false-positive gene-category enrichment in the analysis of spatially resolved transcriptomic brain atlas data. *Nat.*

Commun. **12**, 2669 (2021).

61. Langlieb, J. *et al.* The molecular cytoarchitecture of the adult mouse brain. *Nature* **624**, 333–342 (2023).
62. Siletti, K. *et al.* Transcriptomic diversity of cell types across the adult human brain. *Science* **382**, eadd7046 (2023).
63. Oh, S. W. *et al.* A mesoscale connectome of the mouse brain. *Nature* **508**, 207–214 (2014).
64. Djemil, S., Sames, A. M. & Pak, D. T. S. ACh transfers: Homeostatic plasticity of cholinergic synapses. *Cell. Mol. Neurobiol.* **43**, 697–709 (2023).
65. López-Otín, C., Blasco, M. A., Partridge, L., Serrano, M. & Kroemer, G. The hallmarks of aging. *Cell* **153**, 1194–1217 (2013).
66. Parikh, V., Bernard, C. S., Naughton, S. X. & Yegla, B. Interactions between Aβ oligomers and presynaptic cholinergic signaling: age-dependent effects on attentional capacities. *Behav. Brain Res.* **274**, 30–42 (2014).
67. Baker-Nigh, A. *et al.* Neuronal amyloid-beta accumulation within cholinergic basal forebrain in ageing and Alzheimer's disease. *Brain* **138**, 1722–1737 (2015).
68. Ferreira, S. T., Lourenco, M. V., Oliveira, M. M. & De Felice, F. G. Soluble amyloid-β oligomers as synaptotoxins leading to cognitive impairment in Alzheimer's disease. *Front. Cell. Neurosci.* **9**, 191 (2015).
69. Kadamangudi, S. *et al.* Amyloid-β oligomers increase the binding and internalization of tau oligomers in human synapses. *Acta Neuropathol.* **149**, 2 (2024).
70. Ovsepian, S. V. *et al.* Neurotrophin receptor p75 mediates the uptake of the amyloid beta (Aβ) peptide, guiding it to lysosomes for degradation in basal forebrain cholinergic neurons. *Brain Struct. Funct.* **219**, 1527–1541 (2014).
71. Sotthibundhu, A. *et al.* β-amyloid$_{1–42}$ induces neuronal death through the p75 neurotrophin receptor. *J. Neurosci.* **28**, 3941–3946 (2008).

72. Cohen, A. D. *et al.* Fluid and PET biomarkers for amyloid pathology in Alzheimer's disease. *Mol. Cell. Neurosci.* **97**, 3–17 (2019).

73. Sepulcre, J. *et al.* Neurogenetic contributions to amyloid beta and tau spreading in the human cortex. *Nat. Med.* **24**, 1910–1918 (2018).

74. Grothe, M. J. *et al.* Molecular properties underlying regional vulnerability to Alzheimer's disease pathology. *Brain* **141**, 2755–2771 (2018).

75. Skirzewski, M. *et al.* Continuous cholinergic-dopaminergic updating in the nucleus accumbens underlies approaches to reward-predicting cues. *Nat. Commun.* **13**, 7924 (2022).

76. Longfield, S. F. *et al.* Tau forms synaptic nano-biomolecular condensates controlling the dynamic clustering of recycling synaptic vesicles. *Nat. Commun.* **14**, 7277 (2023).

77. Tracy, T. E. *et al.* Tau interactome maps synaptic and mitochondrial processes associated with neurodegeneration. *Cell* **185**, 712–728.e14 (2022).

78. McInnes, J. *et al.* Synaptogyrin-3 mediates presynaptic dysfunction induced by tau. *Neuron* **97**, 823–835.e8 (2018).

79. Zhou, L. *et al.* Tau association with synaptic vesicles causes presynaptic dysfunction. *Nat. Commun.* **8**, 15295 (2017).

80. Braak, H., Del Tredici, K., Schultz, C. & Braak, E. Vulnerability of select neuronal types to Alzheimer's disease. *Ann. N. Y. Acad. Sci.* **924**, 53–61 (2000).

81. Mesulam, M.-M. Neuroplasticity failure in Alzheimer's disease. *Neuron* **24**, 521–529 (1999).

82. Mesulam, M. M. A plasticity-based theory of the pathogenesis of Alzheimer's disease. *Ann. N. Y. Acad. Sci.* **924**, 42–52 (2000).

83. Arendt, T., Brückner, M. K., Gertz, H. J. & Marcova, L. Cortical distribution of neurofibrillary tangles in Alzheimer's disease matches the pattern of neurons that retain

their capacity of plastic remodelling in the adult brain. *Neuroscience* **83**, 991–1002 (1998).

84. Bossers, K. *et al.* Concerted changes in transcripts in the prefrontal cortex precede neuropathology in Alzheimer's disease. *Brain* **133**, 3699–3723 (2010).
85. Svenningsson, A. L. *et al.* Biological mechanisms of resilience to tau pathology in Alzheimer's disease. *Alzheimers. Res. Ther.* **16**, 221 (2024).
86. Crary, J. F. *et al.* Primary age-related tauopathy (PART): a common pathology associated with human aging. *Acta Neuropathol.* **128**, 755–766 (2014).
87. Hanna Al-Shaikh, F. S. *et al.* Selective Vulnerability of the Nucleus Basalis of Meynert Among Neuropathologic Subtypes of Alzheimer Disease. *JAMA Neurol.* **77**, 225–233 (2019).
88. Shanks, H. R. C., Onuska, K. M., Massa, S. M., Schmitz, T. W. & Longo, F. M. Targeting endogenous mechanisms of brain resilience for the treatment and prevention of Alzheimer's disease. *J. Prev. Alzheimers Dis.* **10**, 699–705 (2023).
89. Randolph, C., Tierney, M. C., Mohr, E. & Chase, T. N. The Repeatable Battery for the Assessment of Neuropsychological Status (RBANS): preliminary clinical validity. *J. Clin. Exp. Neuropsychol.* **20**, 310–319 (1998).
90. Shanks, H. R. C. *et al.* p75 neurotrophin receptor modulation in mild to moderate Alzheimer disease: a randomized, placebo-controlled phase 2a trial. *Nat. Med.* **30**, 1761–1770 (2024).
91. Ashburner, J. & Ridgway, G. R. Symmetric diffeomorphic modeling of longitudinal structural MRI. *Front. Neurosci.* **6**, 197 (2012).
92. German-Castelan, L. *et al.* Sex-dependent cholinergic effects on amyloid pathology: A translational study. *Alzheimers. Dement.* **20**, 995–1012 (2024).
93. Gaser, C. *et al.* CAT: a computational anatomy toolbox for the analysis of structural MRI data. *Gigascience* **13**, (2024).

94. Lorio, S. *et al.* New tissue priors for improved automated classification of subcortical brain structures on MRI. *Neuroimage* **130**, 157–166 (2016).

95. Ashburner, J. & Friston, K. J. Diffeomorphic registration using geodesic shooting and Gauss–Newton optimisation. *Neuroimage* **55**, 954–967 (2011).

96. Mulholland, G. K., Jung, Y.-W., Wieland, D. M., Kilbourn, M. R. & Kuhl, D. E. Synthesis of [18F]fluoroethoxy-benzovesamicol, a radiotracer for cholinergic neurons. *J. Labelled Comp. Radiopharm.* **33**, 583–591 (1993).

97. Yakoub, Y. *et al.* Longitudinal blood biomarker trajectories in preclinical Alzheimer's disease. *Alzheimers. Dement.* **19**, 5620–5631 (2023).

98. de Jong, H. W. A. M. *et al.* Performance evaluation of the ECAT HRRT: an LSO-LYSO double layer high resolution, high sensitivity scanner. *Phys. Med. Biol.* **52**, 1505–1526 (2007).

99. Sibomana, M., Keller, S. H., Stute, S. & Comtat, C. Benefits of 3D scatter correction for the HRRT - a large axial FOV PET scanner. in *2012 IEEE Nuclear Science Symposium and Medical Imaging Conference Record (NSS/MIC)* 2954–2957 (IEEE, 2012).

100. Kanel, P. *et al.* Cerebral topography of vesicular cholinergic transporter changes in neurologically intact adults: A [18F]FEOBV PET study. *Aging Brain* **2**, 100039 (2022).

101. Huber, P. J. *Robust Statistics*. (John Wiley & Sons, Nashville, TN, 1981).

102. Chakraborty, S. *et al.* Multimodal gradients of basal forebrain connectivity across the neocortex. *Nat. Commun.* **15**, 8990 (2024).

103. de Castro, B. M. *et al.* The vesicular acetylcholine transporter is required for neuromuscular development and function. *Mol. Cell. Biol.* **29**, 5238–5250 (2009).

104. Naumova, A. V., Akulov, A. E., Khodanovich, M. Y. & Yarnykh, V. L. High-resolution three-dimensional macromolecular proton fraction mapping for quantitative neuroanatomical imaging of the rodent brain in ultra-high magnetic fields. *Neuroimage*

147, 985–993 (2017).

105. Hikishima, K. *et al.* In vivo microscopic voxel-based morphometry with a brain template to characterize strain-specific structures in the mouse brain. *Sci. Rep.* **7**, 85 (2017).
106. Li, C., Gore, J. C. & Davatzikos, C. Multiplicative intrinsic component optimization (MICO) for MRI bias field estimation and tissue segmentation. *Magn. Reson. Imaging* **32**, 913–923 (2014).
107. Malone, I. B. *et al.* Accurate automatic estimation of total intracranial volume: A nuisance variable with less nuisance. *Neuroimage* **104**, 366–372 (2015).
108. Logan, J. *et al.* Graphical Analysis of Reversible Radioligand Binding from Time—Activity Measurements Applied to [N-11C-Methyl]-(−)-Cocaine PET Studies in Human Subjects. *J. Cereb. Blood Flow Metab.* **10**, 740–747 (1990).
109. Prado, V. F. *et al.* Mice deficient for the vesicular acetylcholine transporter are myasthenic and have deficits in object and social recognition. *Neuron* **51**, 601–612 (2006).
110. Mar, A. C. *et al.* The touchscreen operant platform for assessing executive function in rats and mice. *Nat. Protoc.* **8**, 1985–2005 (2013).
111. Beraldo, F. H. *et al.* MouseBytes, an open-access high-throughput pipeline and database for rodent touchscreen-based cognitive assessment. *Elife* **8**, (2019).
112. Viladomat, J., Mazumder, R., McInturff, A., McCauley, D. J. & Hastie, T. Assessing the significance of global and local correlations under spatial autocorrelation: a nonparametric approach. *Biometrics* **70**, 409–418 (2014).
113. Burt, J. B., Helmer, M., Shinn, M., Anticevic, A. & Murray, J. D. Generative modeling of brain maps with spatial autocorrelation. *Neuroimage* **220**, 117038 (2020).
114. Mathys, H. *et al.* Single-cell atlas reveals correlates of high cognitive function, dementia, and resilience to Alzheimer's disease pathology. *Cell* **186**, 4365–4385.e27 (2023).

Extended Data

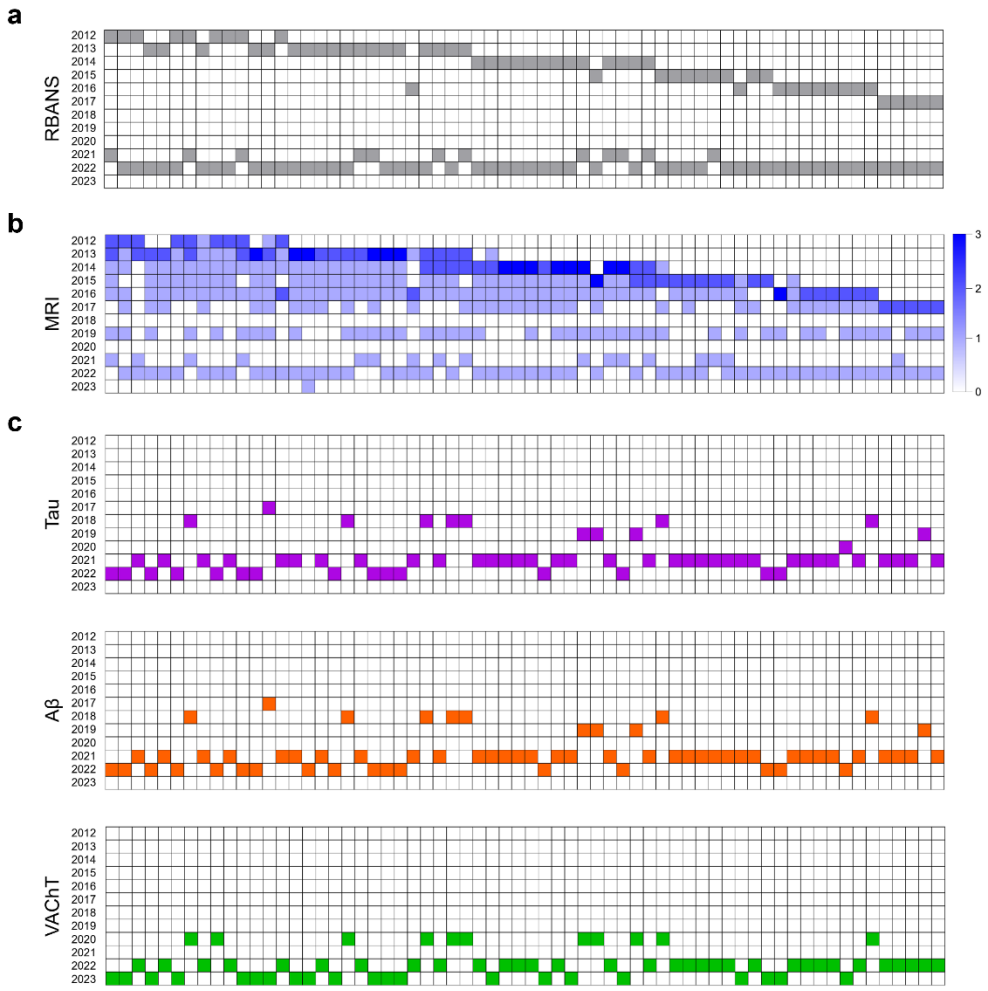

Extended Data Fig. 1. Human data collection timelines.

a, Plot showing the year that participants (*n*=64) underwent baseline and most recent RBANS testing. **b,** Plot showing the years that participants (*n*=64) underwent structural MRI. Darker grid colours indicate a higher number of scans in the corresponding year. **c,** Plots showing the year that participants (*n*=64) underwent tau (*top*; purple), Aβ (*middle*; orange), and VAChT (*bottom*; green) PET imaging.

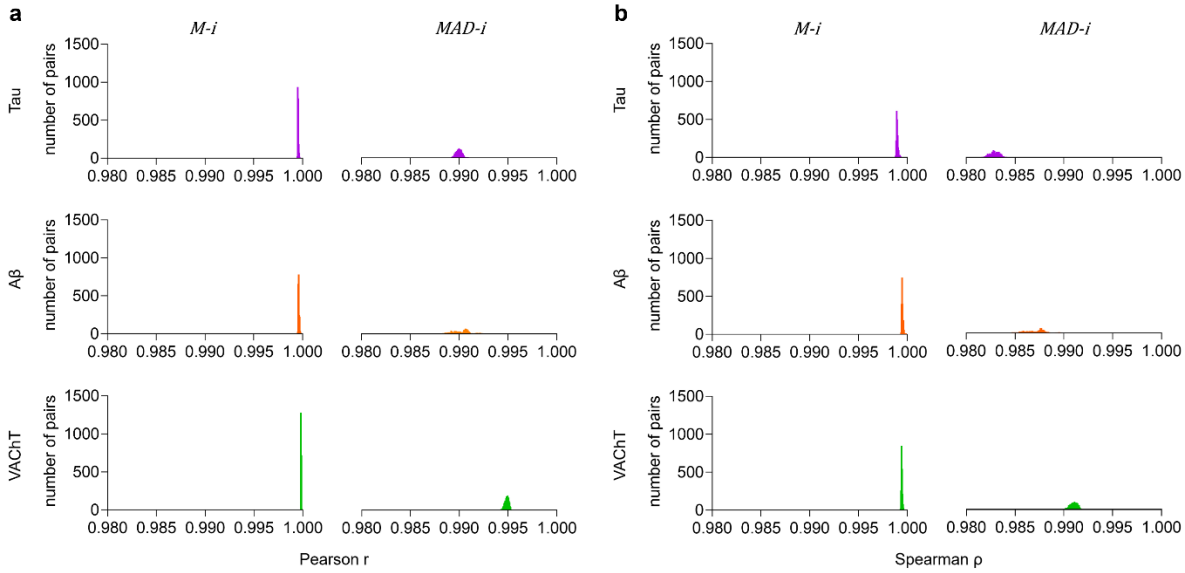

Extended Data Fig. 2. Stability results for Tau-PET, Aβ-PET, and VAChT-PET *M-i* and *MAD-i* population reference images.

a,b, Histograms showing the distribution of Pearson r (**a**) or Spearman ρ (**b**) correlation coefficients between all possible paired-combinations (*n*=2016) of Tau (*top*; purple), Aβ (*middle*; orange), and VAChT (*bottom*; green) *M-i* or *MAD-i* population reference PET images. Source data in **Source Data** file.

Extended Data Fig. 3. Individual Tau-PET normative median deviation mapping profiles.

Segmented normative deviation regions of interest (ROIs) for Tau-PET images *(n*=64), projected on medial and lateral brain surfaces. ROIs are colour coded according to the corresponding confidence interval (CI) bin (<L95=dark blue; L95–M=light blue; M–U95=light red; >U95=dark red).

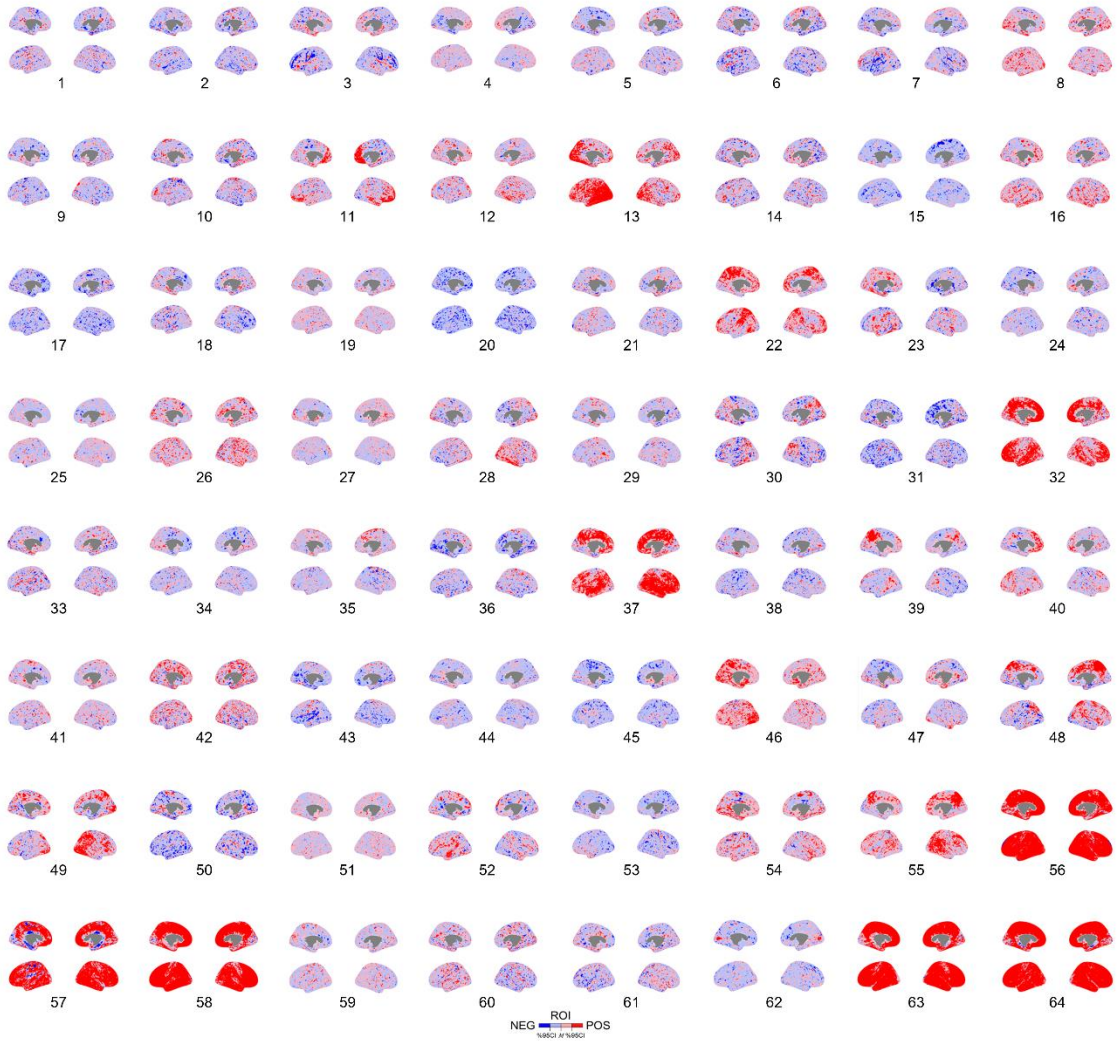

Extended Data Fig. 4. Individual Aβ-PET normative median deviation mapping profiles.

Segmented normative deviation regions of interest (ROIs) for Aβ-PET images *(n*=64), projected on medial and lateral brain surfaces. ROIs are colour coded according to the corresponding confidence interval (CI) bin (<L95=dark blue; L95-M=light blue; M-U95=light red; >U95=dark red).

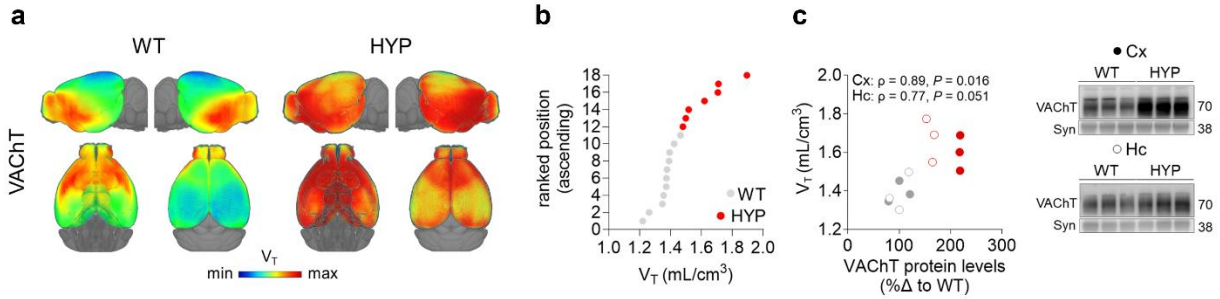

Extended Data Fig. 5. [^{18}F]-FEOBV uptake reflects endogenous increases in synaptic VAChT levels.

a, Representative [^{18}F]-FEOBV total volume of distribution (V_T) images for WT (*left*) and HYP (*right*) mice (min-max: 0.3–2.1). **b,** Scatter plot showing individual mean [^{18}F]-FEOBV V_T values in the mouse BFpz, ranked from lowest to highest (WT: *n*=11, grey; HYP: *n*=7, red) (two-sided Mann-Whitney U test). **c,** Scatter plot between VAChT protein levels measured by Western blots in cortical (Cx, closed circle) and hippocampal (Hc, open circle) tissue from a subset of WT (*n*=3, grey) and HYP (*n*=3, red) mice, and [^{18}F]-FEOBV V_T values in the corresponding brain region (one-sided Spearman rank correlations). Synaptophysin (Syn) is used as a loading control. Example mouse data displayed using MRIcroGL: https://www.nitrc.org/projects/mricrogl. Statistical details in **Supplemental Information Table 1**. Source data in **Source Data** file.

Extended Data Fig. 6. Individual VAChT-PET normative median deviation mapping profiles.

Segmented normative deviation regions of interest (ROIs) for VAChT-PET images *(n*=64), projected on medial and lateral brain surfaces. ROIs are colour coded according to the corresponding confidence interval (CI) bin (<L95=dark blue; L95-M=light blue; M-U95=light red; >U95=dark red).

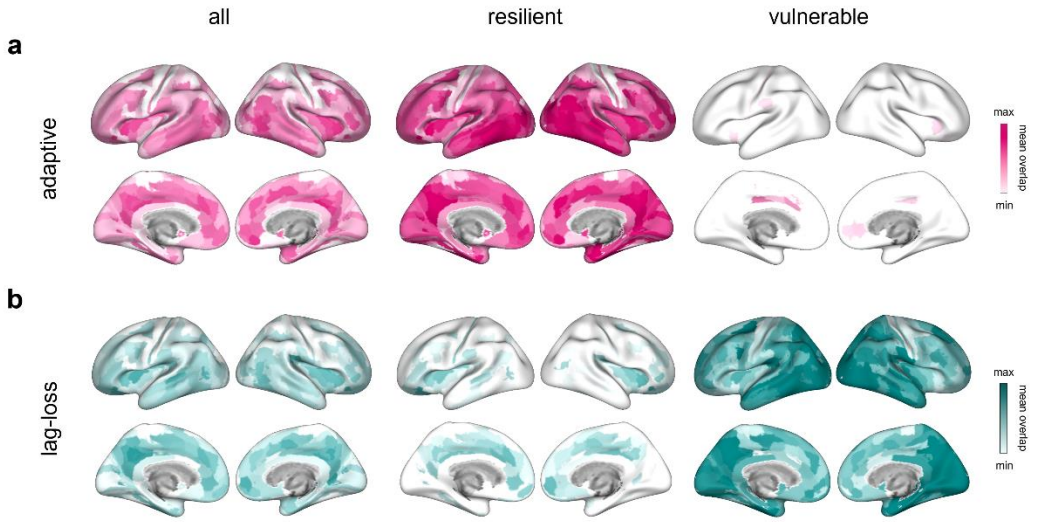

Extended Data Fig. 7. Adaptive and lag-loss models of tau-VAChT colocalization in healthy older adults at risk for Alzheimer's disease.

a,b, Medial and lateral brain surfaces showing the mean overlap of adaptive (**a**) and lag-loss (**b**) model expression in the BFpz across all participants (*n*=64; min-max: 0.2–0.25), resilient individuals (*n*=52; min-max: 0.2–0.25), and vulnerable individuals (*n*=12; min-max: 0.2–0.3). Parcels are from the Human Connectome Project Multi-Modal Parcellation-extended atlas[49]. Source data in **Source Data** file.

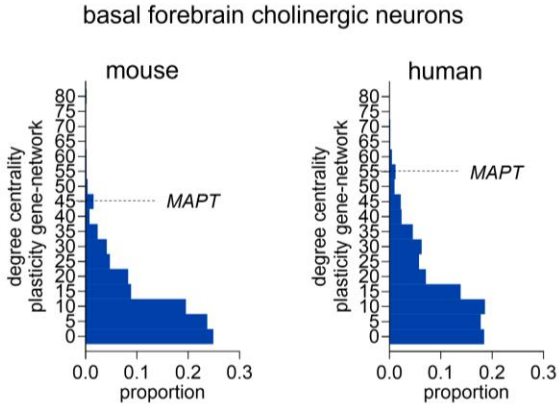

Extended Data Fig. 8. *MAPT* exhibits a high degree of plasticity-gene-network centrality in basal forebrain cholinergic neurons in mice and humans.

Histograms showing the distribution of degree centrality values for 'Module C' genes from Roussarie *et al.*[59] based on their expression in basal forebrain cholinergic neurons in the healthy adult mouse[61] (*left*) and human[62] (*right*) brain. The dotted line indicates the degree centrality bin for the *MAPT* gene. Source data in **Source Data** file.